Prepared for submission to JHEP

Higgs phenomenology in the Stealth Doublet Model

Rikard Enberg,[a] **Johan Rathsman**[b] **and Glenn Wouda**[a]

[a] *Department of Physics and Astronomy, Uppsala University, Box 516, SE–751 20 Uppsala, Sweden*
[b] *Department of Astronomy and Theoretical Physics, Lund University, SE–223 62 Lund, Sweden*
E-mail: Rikard.Enberg@physics.uu.se, Johan.Rathsman@thep.lu.se, Glenn.Wouda@physics.uu.se

Abstract:

We analyze a model for the Higgs sector with two scalar doublets and a softly broken $\mathbb{Z}_2$ symmetry. One of the doublets breaks the electroweak symmetry and has tree-level Yukawa couplings to fermions. The other doublet has no vacuum expectation value and no tree-level couplings to fermions. Because the $\mathbb{Z}_2$ parity is broken the two doublets can mix, which leads to a distinct and novel phenomenology. This Stealth Doublet Model can be seen as a generalization of the Inert Doublet Model with a broken $\mathbb{Z}_2$ symmetry. We outline the model and present constraints from theory, electroweak precision tests and collider searches, including the recent observation of a Higgs boson at the LHC. The CP-odd scalar A and the charged scalar $H^\pm$ couple to fermions at one-loop level. We compute the decays of A and $H^\pm$ and in particular the one-loop decays $A \to f\bar{f}$, $H^\pm \to f\bar{f}'$, $H^\pm \to W^\pm Z$ and $H^\pm \to W^\pm\gamma$. We also describe how to calculate and renormalize such processes in our model. We find that if one of $H^\pm$ or A is the lightest scalar, $H^\pm \to W^\pm\gamma$ or $A \to b\bar{b}$ are typically their respective dominating decay channels. Otherwise, the dominating decays of $H^\pm$ and A are into a scalar and a vector. Due to the absence of tree-level fermion couplings for $H^\pm$ and A, we consider pair production and associated production with vector bosons and scalars at the LHC. If the parameter space of the model that favors $H^\pm \to W^\pm\gamma$ is realized in Nature, we estimate that there should be a considerable amount of such events in the present LHC data.

Contents

1 Introduction

The ATLAS [1] and CMS [2, 3] experiments at the Large Hadron Collider (LHC) have after a long history of searches discovered a Higgs boson. By all accounts the properties of the observed particle agree very well with what is expected of a Standard Model (SM) Higgs boson (see e.g. [4–7] for more recent data), but it will require much work to ascertain whether the SM Higgs doublet is all there is, or if an extended Higgs sector exists. There are some, although not quite significant, hints of an enhanced signal strength in $H \to \gamma\gamma$ from ATLAS, but CMS sees no such an effect. It is important to now probe and investigate the Higgs sector in detail to understand the observations and what can be expected.

Much work has been dedicated to studying some standard scenarios for the electroweak symmetry breaking sector. Among these scenarios are the SM, the Minimal Supersymmetric Standard Model (MSSM), and general CP-conserving two-Higgs doublet models (2HDMs). For the latter models one often imposes a, possibly softly broken, $\mathbb{Z}_2$ symmetry to prevent the occurrence of large flavor-changing neutral currents (FCNCs). General 2HDMs have been recently reviewed in Ref. [8]. Except for the SM, these models predict a set of additional Higgs bosons, each of which has characteristic production and decay channels for a given set of parameters.

In general models with two Higgs doublets there are two CP-even neutral Higgs bosons, h and H, which have the same couplings to fermions and gauge bosons (up to mixing angles) as the SM Higgs. Their decay channels are the same as for the SM Higgs plus possible decays to lighter Higgs bosons. Of course their branching ratios can be very different because of different coupling strengths and different open decay channels. There is additionally a CP-odd neutral Higgs boson A, which mainly decays to the heaviest possible fermions, $A \to b\bar{b}$ or $t\bar{t}$, or to a Higgs-vector boson pair, $A \to hZ$, $H^\pm W^\mp$. Finally, there is a charged Higgs boson $H^\pm$, which depending on its mass decays mainly as $H^\pm \to \tau\nu$, cs or tb, or as $H^\pm \to hW^\pm$ or $H^\pm \to AW^\pm$.

An alternative scenario is presented by the Inert Doublet Model (IDM) [9–11], where there is a SM-like Higgs boson, but in addition there is another doublet that is odd under a discrete $\mathbb{Z}_2$ symmetry. Making all other SM particles even under this symmetry and demanding that the Lagrangian is $\mathbb{Z}_2$ symmetric, the scalars from the other doublet become fermiophobic and do not couple to fermions. Thus, if the $\mathbb{Z}_2$ symmetry is exact the lightest scalar from this doublet is stable, providing a possible dark matter candidate (see e.g. [12, 13] for constraints on the IDM from dark matter). This makes for a very different phenomenology, so that if an alternative scenario such as the IDM or some other non-standard model is realized in Nature, the common searches may prove inadequate.

The Stealth Doublet Model (SDM) studied in this paper was recently proposed in Ref. [14]. It can be seen as a generalization of the IDM, but with the $\mathbb{Z}_2$ symmetry softly broken in the scalar potential. This means that, in general, there is no stable scalar particle, but instead there are now two particles, h and H, that can play the role of the Higgs boson observed at LHC. In [14] we showed that this model can describe the observations of ATLAS and CMS very well. In this paper we will study the model in more detail, and we will in particular study some of the properties of the charged scalar $H^\pm$ and the CP-odd scalar A.

As in the IDM, the A and $H^\pm$ have no tree-level couplings to fermions, and must therefore be produced and decay in different channels than in the standard scenarios. However, contrary to the IDM, because of the softly broken $\mathbb{Z}_2$ symmetry, couplings to fermions are now generated at the one-loop level. The usual decay channels of the A and $H^\pm$ bosons into fermions are therefore loop suppressed in our model. Consequently, model-dependent constraints do not always apply, and A and $H^\pm$ can be lighter in our model than in standard scenarios. For example, the main decay of the charged Higgs is typically $H^\pm \to W^\pm\gamma$, provided that $H^\pm$ is the lightest scalar. Another example is that the production of the CP-odd Higgs A through gluon-gluon fusion is strongly suppressed, but still the main decay channel is typically into $b\bar{b}$ as in the standard scenarios.

Fermiophobic models have been discussed previously [15–21], for the case where the lightest CP-even Higgs boson is fermiophobic. Such a Higgs boson has an increased branching ratio for $h \to \gamma\gamma$ but is not produced in $gg \to h$. In our model, instead, the lightest CP-even Higgs boson has the same types of interactions as in standard 2HDMs, but the A and $H^\pm$ are fermiophobic. Fermiophobic charged Higgs bosons have recently also been discussed in [22].

If a symmetry is only broken by dimension-two mass terms, it is said to be softly broken, and the symmetry is then restored in the high energy limit. Such soft symmetry breaking in the Higgs sector is discussed in [23–26]. In particular, we in this paper consider soft breaking of the discrete $\mathbb{Z}_2$ symmetry as a way to parametrize our ignorance of the symmetry breaking mechanism. This is the conventional approach in supersymmetric (SUSY) models with soft SUSY breaking terms in the Lagrangian. For an explicit example of a UV complete model with composite Higgs bosons that leads to a similar type of 2HDM that we are considering here, see [27].

As already mentioned, a $\mathbb{Z}_2$ symmetry is usually imposed on 2HDMs in order to not run into dangerous FCNCs. One possibility is to arrange the symmetry such that only one of the doublets couples to fermions. This is known as a Type-I Yukawa sector, and our model is an example of such a Yukawa sector. An additional motivation for considering Type-I models is that recent work in string theory [28] seems to imply that they are generic in heterotic string theories, where selection rules forbid additional Higgs doublets from coupling to fermions. Type-I models by definition have an exact $\mathbb{Z}_2$ symmetry in the Yukawa sector. As a consequence, if the symmetry is broken softly in the Higgs potential, then no dangerous FCNCs are generated at tree-level, as the symmetry is restored at high energies. This also applies to our model, where new sources of FCNCs only appear at the two-loop level.

The organization of this paper is as follows: in section 2 we discuss the definition of the model and derive masses and couplings. In particular, we discuss the parametrization of the soft $\mathbb{Z}_2$ breaking and the free parameters of the model. We then consider constraints on the model from theoretical considerations and electroweak precision tests (EWPT) in section 3. The recently observed Higgs boson at the LHC is discussed in the context of our model in section 4. Decays of the scalar particles are discussed in section 5. Finally, we briefly discuss the collider phenomenology of the charged scalar and the CP-odd scalar in section 6. Some more technical matters are relegated to the appendices.

2 The Stealth Doublet Model

In this section we will analyze the scalar potential of the model, derive the mass eigenstates, and consider the free parameters and the constraints put on them from the requirement that the $\mathbb{Z}_2$ symmetry is softly broken. We will in the following refer to the model as the Stealth Doublet Model (SDM). The model has previously been presented in [14] and in the conference proceedings [29].

2.1 The scalar potential

We introduce two $\mathrm{SU}(2)_L$-doublet, hypercharge $Y = 1$, complex scalar fields $\Phi_{1,2}$, which may be written in terms of their component fields as

$$\Phi_{1,2} = \begin{pmatrix} \varphi_{1,2}^+ \\ \varphi_{1,2} \end{pmatrix}, \tag{2.1}$$

or in components $[\Phi_{1,2}]^+ = \varphi_{1,2}^+$ and $[\Phi_{1,2}]^0 = \varphi_{1,2}$. We then consider the most general gauge invariant and renormalizable scalar potential,

$$\begin{aligned} \mathcal{V}[\Phi_1, \Phi_2] = {} & m_{11}^2 \Phi_1^\dagger \Phi_1 + m_{22}^2 \Phi_2^\dagger \Phi_2 - [m_{12}^2 \Phi_1^\dagger \Phi_2 + \text{h.c.}] \\ & + \frac{1}{2}\lambda_1 (\Phi_1^\dagger \Phi_1)^2 + \frac{1}{2}\lambda_2 (\Phi_2^\dagger \Phi_2)^2 + \lambda_3 (\Phi_1^\dagger \Phi_1)(\Phi_2^\dagger \Phi_2) + \lambda_4 (\Phi_1^\dagger \Phi_2)(\Phi_2^\dagger \Phi_1) \\ & + \left\{ \frac{1}{2}\lambda_5 (\Phi_1^\dagger \Phi_2)^2 + \left[\lambda_6 (\Phi_1^\dagger \Phi_1) + \lambda_7 (\Phi_2^\dagger \Phi_2)\right] \Phi_1^\dagger \Phi_2 + \text{h.c.} \right\}, \end{aligned} \tag{2.2}$$

where all parameters are real except $\lambda_{5,6,7}$ and m_{12}^2, which may be complex. In this paper we are only concerned with CP-conserving models and will from now on assume all couplings to be real.

There is a priori no difference between the two fields Φ_1 and Φ_2 in the potential (2.2), which is invariant under global $\mathrm{U}(2)$ transformations of the two doublets, $\Phi_a \to U_{ab}\Phi_b$ with $U \in \mathrm{U}(2)$. We may define a basis for the doublets in terms of their vacuum expectation values (vevs) as

$$\langle \Phi_1 \rangle = \begin{pmatrix} 0 \\ v_1 \end{pmatrix} \tag{2.3}$$

$$\langle \Phi_2 \rangle = \begin{pmatrix} 0 \\ v_2\, e^{\mathrm{i}\xi} \end{pmatrix}, \tag{2.4}$$

where $v^2 = v_1^2 + v_2^2 \approx (246\,\mathrm{GeV})^2$ is the total vev, and where ξ is a possible phase that could allow spontaneous CP breaking, which we therefore set to zero. A $\mathrm{U}(2)$ transformation may then be seen as a change of basis, where the total vev is rotated between the doublets. The traditional parameter $\tan\beta = v_2/v_1$, which is a physical parameter in the MSSM at tree-level, does therefore not in general have a physical meaning. It is only after specifying the structure of the Yukawa couplings to fermions that a basis is singled out as the physical basis. A particular choice of basis is $v_2 = 0$, i.e., the vacuum expectation value resides completely in Φ_1. This is known as the Higgs basis in the literature, and our model is a physical realization of this basis (see [8, 24, 26] for clear discussions of basis changes and

the Higgs basis). In this basis there is naturally no $\tan\beta$ parameter, and we shall not use it.

The potential (2.2) explicitly breaks the $\mathbb{Z}_2$ symmetry

$$\Phi_1 \to \Phi_1 \tag{2.5}$$

$$\Phi_2 \to -\Phi_2 \tag{2.6}$$

through the dimension-two operator $\Phi_1^\dagger\Phi_2$+h.c. with coupling m_{12}^2 and the dimension-four operators $(\Phi_1^\dagger\Phi_1)(\Phi_1^\dagger\Phi_2)$+h.c. and $(\Phi_2^\dagger\Phi_2)(\Phi_1^\dagger\Phi_2)$+h.c. with couplings λ_6 and λ_7. Such a $\mathbb{Z}_2$ symmetry is often imposed to remove these terms. It is also imposed, with various schemes for assignments of $\mathbb{Z}_2$ charges to fermions, in order to forbid large flavor-changing neutral currents (FCNC) [30, 31], by arranging the Yukawa couplings such that each fermion only couples to one doublet.

The dimension-four operators lead to hard breaking of the $\mathbb{Z}_2$ symmetry, while the dimension-two operator breaks it softly, meaning that at very high energies, $E^2 \gg |m_{12}^2|$, the symmetry is restored [32]. If the symmetry is broken, large FCNC may potentially occur, but we will only encounter new sources of FCNC at the two-loop level (see section 2.4 below).

We will thus consider a physical realization of the Higgs basis where only Φ_1 couples to fermions and acquires a vev at tree-level, i.e. $v_1 = v \approx 246$ GeV. The minimization conditions for electroweak symmetry breaking are simple,

$$m_{11}^2 = -\frac{1}{2}v^2\lambda_1, \tag{2.7}$$

$$m_{12}^2 = \frac{1}{2}v^2\lambda_6, \tag{2.8}$$

giving no constraint on m_{22}^2, which is therefore a free parameter in our model.

We must also consider bounds on the parameters from the requirement that the potential is bounded from below [9, 33]. Stability of the potential gives rise to a number of constraints on the parameters in the quartic part of the potential. The simplest constraints are

$$\lambda_1 > 0, \qquad \lambda_2 > 0, \qquad \lambda_3 > -\sqrt{\lambda_1\lambda_2}, \qquad \lambda_3 + \lambda_4 - \lambda_5 > -\sqrt{\lambda_1\lambda_2}, \tag{2.9}$$

where the last equation applies for $\lambda_6 \neq 0$ or $\lambda_7 \neq 0$. There are also additional constraints that we do not list here, which can be found in references [9, 33]. In addition, one can also constrain the parameters by requiring perturbativity of the various four-Higgs couplings and tree-level unitarity as we will come back to below in section 3.

2.2 Physical states and mass relations

We choose Φ_1 to be the doublet that gets a vev, with $\mathbb{Z}_2$ parity $+1$, and Φ_2 to be the one with zero vev and $\mathbb{Z}_2$ parity -1. In a CP-conserving 2HDM, there are two CP-even neutral states h, H, one CP-odd neutral state A, and two charged states $H^\pm$. We may write the

doublets as

$$\Phi_1 = \frac{1}{\sqrt{2}}\begin{pmatrix} \sqrt{2}G^+ \\ v + \phi_1 + \mathrm{i}G^0 \end{pmatrix} \tag{2.10}$$

$$\Phi_2 = \frac{1}{\sqrt{2}}\begin{pmatrix} \sqrt{2}H^+ \\ \phi_2 + \mathrm{i}A \end{pmatrix}, \tag{2.11}$$

where $G^\pm$ and G^0 are the Goldstone bosons and $\phi_{1,2}$ are the neutral CP-even interaction eigenstates. The doublet Φ_2 is fermiophobic, i.e., the states $H^\pm$, A, and ϕ_2 do not interact with fermions at tree-level. Because only Φ_1 acquires a vacuum expectation value, we do not call Φ_2 a "Higgs" doublet. From now on, we will also call the mass eigenstates in our model "scalars", not Higgs bosons, in accordance with the usual IDM nomenclature [11].

The masses for the A and $H^\pm$ can be found directly from the potential,

$$m_A^2 = m_{22}^2 + \frac{1}{2}v^2(\lambda_3 + \lambda_4 - \lambda_5) = m_{H^\pm}^2 - \frac{1}{2}v^2(\lambda_5 - \lambda_4) \tag{2.12}$$

$$m_{H^\pm}^2 = m_{22}^2 + \frac{1}{2}v^2\lambda_3. \tag{2.13}$$

The mass matrix for the CP-even states has non-diagonal elements, and we may find the physical mass eigenstates by diagonalizing this matrix. Taking the minimization conditions (2.7, 2.8) into account, we have

$$\mathcal{M}^2 = \begin{pmatrix} \lambda_1 v^2 & \lambda_6 v^2 \\ \lambda_6 v^2 & m_{22}^2 + \lambda_{345} v^2 \end{pmatrix} = \begin{pmatrix} \lambda_1 v^2 & \lambda_6 v^2 \\ \lambda_6 v^2 & m_A^2 + \lambda_5 v^2 \end{pmatrix}, \tag{2.14}$$

where $\lambda_{345} = \lambda_3 + \lambda_4 + \lambda_5$. The matrix $\mathcal{M}^2$ may be diagonalized by an orthogonal matrix V, defined by a rotation angle α, as

$$\begin{pmatrix} m_H^2 & 0 \\ 0 & m_h^2 \end{pmatrix} = V^T \mathcal{M}^2 V. \tag{2.15}$$

The physical CP-even states are then given by (with α defined so that $m_H > m_h$)

$$\begin{pmatrix} H \\ h \end{pmatrix} = V^T \begin{pmatrix} \phi_1 \\ \phi_2 \end{pmatrix} = \begin{pmatrix} \cos\alpha & \sin\alpha \\ -\sin\alpha & \cos\alpha \end{pmatrix} \begin{pmatrix} \phi_1 \\ \phi_2 \end{pmatrix}, \quad \text{where} \quad -\frac{\pi}{2} \leq \alpha \leq \frac{\pi}{2}, \tag{2.16}$$

or, in terms of the doublets,

$$H = \quad (\sqrt{2}\,\mathrm{Re}\,[\Phi_1]^0 - v)\cos\alpha + \sqrt{2}\,\mathrm{Re}\,[\Phi_2]^0 \sin\alpha \tag{2.17}$$

$$h = -(\sqrt{2}\,\mathrm{Re}\,[\Phi_1]^0 - v)\sin\alpha + \sqrt{2}\,\mathrm{Re}\,[\Phi_2]^0 \cos\alpha\,, \tag{2.18}$$

where $[\Phi_{1,2}]^0 = \varphi_{1,2}$, c.f. eq. (2.1). The physical CP-even scalar masses can be expressed as

$$m_h^2 = c_\alpha^2 m_A^2 + s_\alpha^2 v^2 \lambda_1 + c_\alpha^2 v^2 \lambda_5 - 2 s_\alpha c_\alpha v^2 \lambda_6 \tag{2.19}$$

$$m_H^2 = s_\alpha^2 m_A^2 + c_\alpha^2 v^2 \lambda_1 + s_\alpha^2 v^2 \lambda_5 + 2 s_\alpha c_\alpha v^2 \lambda_6, \tag{2.20}$$

where we defined the abbreviations $s_\alpha \equiv \sin\alpha$, $c_\alpha \equiv \cos\alpha$. Finally, we have explicit expressions for the potential parameters $\lambda_{1,3,4,5}$ in terms of the masses, the mixing angle α, and the couplings λ_6 and m_{22}^2,

$$\lambda_1 v^2 = \frac{m_H^2 + m_h^2}{2} + \frac{\left(m_H^2 - m_h^2\right)}{2\cos 2\alpha} - v^2\lambda_6 \tan 2\alpha \tag{2.21}$$

$$\lambda_3 v^2 = 2\left(m_{H^\pm}^2 - m_{22}^2\right) \tag{2.22}$$

$$\lambda_4 v^2 = \frac{m_H^2 + m_h^2}{2} - \frac{\left(m_H^2 - m_h^2\right)}{2\cos 2\alpha} + v^2\lambda_6 \tan 2\alpha + m_A^2 - 2m_{H^\pm}^2 \tag{2.23}$$

$$\lambda_5 v^2 = \frac{m_H^2 + m_h^2}{2} - \frac{\left(m_H^2 - m_h^2\right)}{2\cos 2\alpha} + v^2\lambda_6 \tan 2\alpha - m_A^2, \tag{2.24}$$

allowing us to use the masses of the scalars as parameters of the model. The mixing angle is given by

$$\tan 2\alpha = \frac{2v^2\lambda_6}{v^2(\lambda_1 - \lambda_5) - m_A^2}, \tag{2.25}$$

or, in terms of the masses and λ_6 only,

$$\sin 2\alpha = \frac{2v^2\lambda_6}{m_H^2 - m_h^2}. \tag{2.26}$$

Note that the mass relations eqs. (2.12), (2.13), (2.19) and (2.20) are invariant under $\sin\alpha \to -\sin\alpha$. Equivalently, from eqs. (2.21–2.24), the parameters λ_1, λ_3, λ_4 and λ_5 are invariant. This is easily seen, since as we have $-\frac{\pi}{2} \leq \alpha \leq \frac{\pi}{2}$, the parameter $\sin\alpha$ can take any value $-1 \leq \sin\alpha \leq 1$, and $\cos\alpha$ is always non-negative. This implies that under $\sin\alpha \to -\sin\alpha$, we have $\sin 2\alpha \to -\sin 2\alpha$ and $\lambda_6 \to -\lambda_6$.

Eqs. (2.21–2.24) are not valid in the case of maximal mixing, $\alpha = \pm\frac{\pi}{4}$. In this case one instead obtains

$$\lambda_1 v^2 = \frac{m_H^2 + m_h^2}{2} \tag{2.27}$$

$$\lambda_3 v^2 = 2\left(m_{H^\pm}^2 - m_{22}^2\right) \tag{2.28}$$

$$\lambda_4 v^2 = \frac{m_H^2 + m_h^2}{2} + m_A^2 - 2m_{H^\pm}^2 \tag{2.29}$$

$$\lambda_5 v^2 = \frac{m_H^2 + m_h^2}{2} - m_A^2. \tag{2.30}$$

Eqs. (2.14) and (2.26) show that when the $\mathbb{Z}_2$ symmetry is exact ($\lambda_6 = 0$), the mass matrix is diagonal and there will be no mixing between h and H. This is the case in the Inert Doublet Model; in fact all our results reduce to the IDM in the limit $\lambda_6 \to 0$, $\lambda_7 \to 0$ and $\sin\alpha \to 1$ or -1.[1] In this sense, our model is a generalization of the IDM.

The scalar-scalar couplings depend on the potential parameters and are straightforward to obtain from the potential. The scalar-gauge boson couplings are obtained from the covariant derivatives and depend on the mixing angle only. The relevant three-particle couplings are listed in Appendix A.

[1] Note that in this case the relation $m_H > m_h$ is not valid, since no rotation is performed to diagonalize the mass matrix $\mathcal{M}^2$.

2.3 Soft breaking of the $\mathbb{Z}_2$ symmetry

We have so far imposed the condition of electroweak symmetry breaking and have identified the physical scalars and their masses and mixing. We will now further constrain the potential parameters so that the scalar potential only breaks the $\mathbb{Z}_2$ symmetry softly. Naively, it may seem that because the soft $\mathbb{Z}_2$-breaking parameter m_{12}^2 is proportional to the hard breaking parameter λ_6 (eq. (2.8)), hard breaking is linked to soft breaking. However, there may exist a basis in which $\lambda_6 = \lambda_7 = 0$ while $m_{12}^2 \neq 0$ such that the symmetry is broken softly. If this is the case, then the symmetry is broken softly in any basis reached by a U(2) transformation. To find constraints on the potential parameters for when this is the case, we employ the basis-independent methods of Davidson and Haber [24] (see also [25, 26]). We find that in the Higgs basis the conditions are

$$(\lambda_1 - \lambda_2)\left[\lambda_{345}(\lambda_6 + \lambda_7) - \lambda_2\lambda_6 - \lambda_1\lambda_7\right] - 2(\lambda_6 - \lambda_7)(\lambda_6 + \lambda_7)^2 = 0, \tag{2.31}$$

$$(\lambda_1 - \lambda_2)m_{12}^2 + (\lambda_6 + \lambda_7)(m_{11}^2 - m_{22}^2) \neq 0. \tag{2.32}$$

Eqs.(2.31) and (2.32) define the model parameter space. As explained below in section 2.5, λ_7 will be one of the free parameters of the model, and λ_2 can then be chosen from the second order equation in λ_2 for a given λ_7-value resulting from eq. (2.31):

$$\lambda_2^{(\pm)} = -\frac{B}{2} \pm \sqrt{\frac{B^2}{4} - C}\,, \tag{2.33}$$

where

$$B = -\left[\lambda_1(\lambda_6 - \lambda_7) + \lambda_{345}(\lambda_6 + \lambda_7)\right]/\lambda_6 \tag{2.34}$$

and

$$C = \left[\lambda_1\lambda_{345}(\lambda_6 + \lambda_7) - \lambda_1^2\lambda_7 - 2(\lambda_6 - \lambda_7)(\lambda_6 + \lambda_7)^2\right]/\lambda_6. \tag{2.35}$$

All quartic couplings λ_i that satisfy these relations break the $\mathbb{Z}_2$ symmetry softly, although the fact that the breaking is soft is not manifest. One can visualize the model space by solving the second order equation (2.31) for each value of λ_7 and plotting the resulting roots, see figure 1 for some examples. The behavior of the allowed points is non-trivial. From the requirement that λ_2 is real one also gets a maximum allowed value for λ_7,

$$\lambda_7^{\max} = \lambda_6 + \frac{(\lambda_1 - \lambda_{345})^2}{8\lambda_6}. \tag{2.36}$$

By inspection of eq. (2.31) one obtains that $\lambda_7 = \lambda_6$, $\lambda_2 = \lambda_1$ is always a solution if $m_{22}^2 \neq m_{11}^2$, from eq. (2.32).

2.4 Yukawa sector

We have up to now specified the scalar sector by considering a physical realization of the Higgs basis where only Φ_1 acquires a vev. Furthermore, we imposed a discrete $\mathbb{Z}_2$ symmetry on the scalar doublets and allowed this symmetry to be broken only softly. This can be achieved if the parameters of the scalar potential eq. (2.2) satisfy the relations (2.31) and

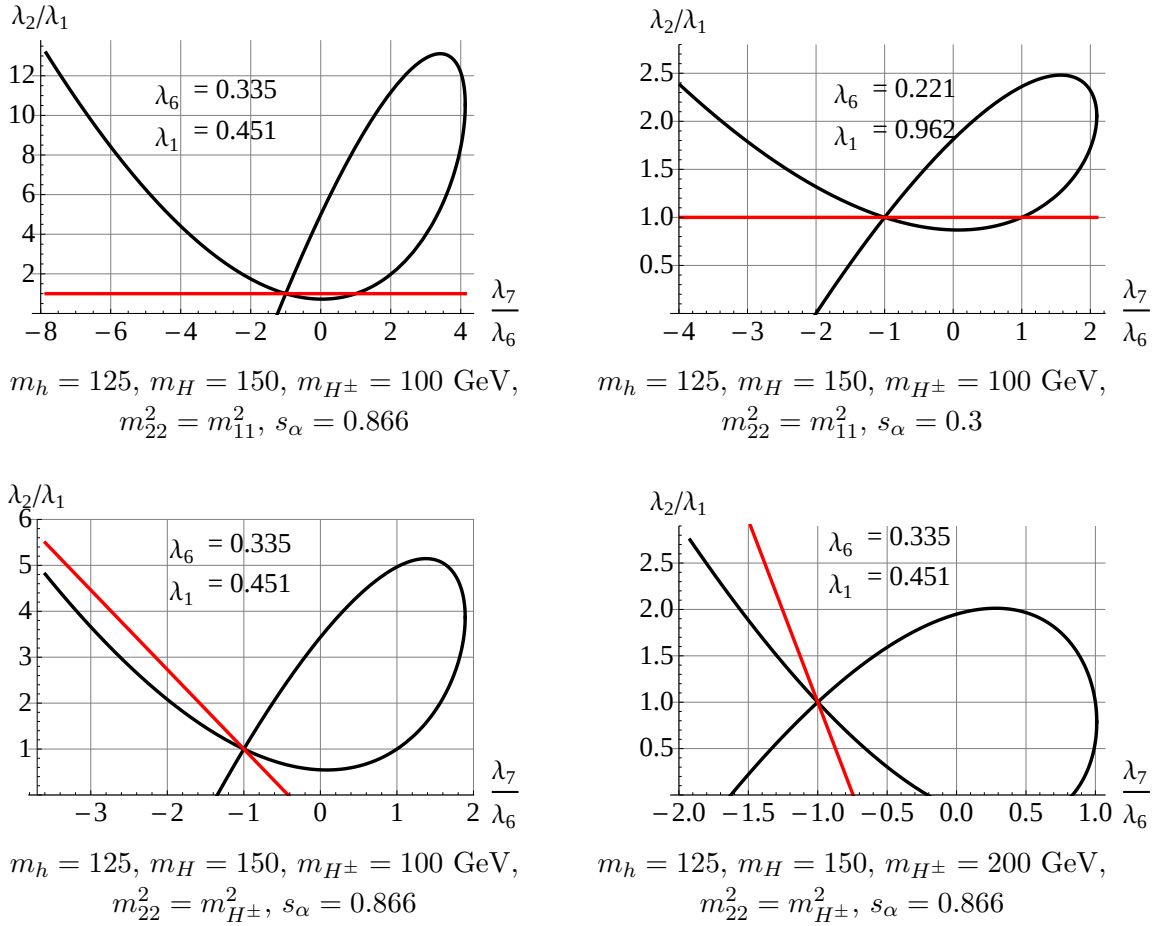

$m_h = 125$, $m_H = 150$, $m_{H^\pm} = 100$ GeV, $m_{22}^2 = m_{11}^2$, $s_\alpha = 0.866$

$m_h = 125$, $m_H = 150$, $m_{H^\pm} = 100$ GeV, $m_{22}^2 = m_{11}^2$, $s_\alpha = 0.3$

$m_h = 125$, $m_H = 150$, $m_{H^\pm} = 100$ GeV, $m_{22}^2 = m_{H^\pm}^2$, $s_\alpha = 0.866$

$m_h = 125$, $m_H = 150$, $m_{H^\pm} = 200$ GeV, $m_{22}^2 = m_{H^\pm}^2$, $s_\alpha = 0.866$

Figure 1. The black line displays the allowed values of λ_2 and λ_7 according to eq. (2.31). The red line corresponds to eq. (2.32); these points are not allowed.

(2.32). Now we are in a position to specify the Yukawa couplings of the model. The most general Yukawa Lagrangian in the Higgs basis reads [26]

$$\begin{aligned} -\mathcal{L}_{\text{Yukawa}} &= \kappa_0^L \bar{L}_L \Phi_1 E_R + \kappa_0^U \bar{Q}_L (-\mathrm{i}\sigma_2 \Phi_1^*)\, U_R + \kappa_0^D \bar{Q}_L \Phi_1 D_R \\ &\quad + \rho_0^L \bar{L}_L \Phi_2 E_R + \rho_0^U \bar{Q}_L (-\mathrm{i}\sigma_2 \Phi_2^*)\, U_R + \rho_0^D \bar{Q}_L \Phi_2 D_R \end{aligned} \tag{2.37}$$

and is written in terms of the electroweak interaction eigenstates. In order to obtain the fermion mass eigenstates, the matrices κ_0^F, ρ_0^F $(F = U, D, L)$ are transformed by a biunitary transformation that diagonalizes κ_0^F using the unitary matrices V_L^F, V_R^F according to

$$\kappa^F = V_L^F \kappa_0^F V_R^F = \frac{\sqrt{2}}{v} M^F, \quad \rho^F = V_L^F \rho_0^F V_R^F, \tag{2.38}$$

where M^F is the diagonal mass matrix for fermions F, e.g. $\left[M^L\right]_{22} = m_\mu$ etc. The ρ^F matrices are in general non-diagonal and will generate FCNC. To naturally avoid large FCNC at tree level, we also impose (positive) $\mathbb{Z}_2$ parities to the fermions. This is obtained by enforcing $\rho^F = 0$ at tree level; in other words Φ_2 will not couple to fermions. Thus, our

model is a Type-I 2HDM. The fermions will acquire mass through Yukawa couplings with the Higgs doublet Φ_1 only. The Yukawa Lagrangian in unitary gauge reads

$$-\mathcal{L}_{\text{Yukawa}} = \frac{m_f}{v}\,\bar{\Psi}_f\Psi_f\,(\,H\,\cos\alpha - h\,\sin\alpha\,)\,, \tag{2.39}$$

for all fermions f. As will be shown in sections 5.2.1 and 5.3.1 the soft breaking terms $m_{12}^2\Phi_1^\dagger\Phi_2 +$ h.c. will generate couplings between Φ_2 and fermions, i.e. $\rho^F \neq 0$ at one-loop level. Furthermore, the ρ^F matrices are diagonal at one-loop level. At higher orders in perturbation theory, ρ^F will develop off-diagonal elements and introduce additional sources of FCNC[2]. Finally we also note that the couplings of fermions to A and $H^\pm$ are also governed by ρ^F, more specifically we have terms of the form $\mathrm{i}\bar{F}\rho^F\gamma_5 FA$ and $\bar{U}\left[V_{\text{CKM}}\rho^D(1+\gamma_5) - \rho^U V_{\text{CKM}}(1-\gamma_5)\right]DH^+$.

2.5 Parameters of the model

By imposing CP conservation with only real parameters, the scalar potential has ten free parameters. The minimization conditions (2.7, 2.8) remove m_{11}^2 and m_{12}^2, leaving us with the eight parameters λ_1–λ_7 and m_{22}^2. Finally, the condition for soft $\mathbb{Z}_2$ breaking removes one more parameter. We may use the relations (2.21–2.24) to relate λ_1, λ_3, λ_4, and λ_5 to the four physical scalar masses m_h, m_H, m_A and $m_{H^\pm}$. The parameter λ_6 can be used to specify the amount of $\mathbb{Z}_2$ breaking, but considering eqs. (2.25, 2.26) we choose to instead use the mixing angle α for this purpose, since in a general 2HDM $\sin(\alpha-\beta)$ is invariant under basis changes. Of the remaining λ-parameters λ_2 and λ_7, we note that λ_2 only enters indirectly through the stability and tree-level unitarity constraints, etc., as its only direct effect is to set the strength of the self-interaction of the Φ_2 field. As discussed above, λ_2 can then be specified if we give a value for λ_7, which will be our chosen parameter. Finally, we can relate λ_3 and m_{22}^2 using eq. (2.13). We choose λ_3 as input parameter, as this parameter enters the coupling between the CP-even states and pairs of charged scalars, see sections 4, 5.1, and Appendix A.

The seven parameters of the model that we will use are then

$$m_h,\ m_H,\ m_A,\ m_{H^\pm},\ \sin\alpha,\ \lambda_3,\ \lambda_7.$$

To simplify our analysis we will often make the following assumptions. To start with, we choose $\lambda_2 = \lambda_1$ and $\lambda_7 = \lambda_6$ in order to fulfill the condition (2.31). We will also sometimes be using a set of representative values for λ_3, chosen as $\lambda_3 = 0$, $2m_{H^\pm}^2/v^2$ and $4m_{H^\pm}^2/v^2$, corresponding to $m_{22}^2 = m_{H^\pm}^2$, 0 and $-m_{H^\pm}^2$, respectively. In section 4 we will vary λ_3 and λ_7, within theoretically allowed regions, to deduce their impact on the signal strengths for $h\to\gamma\gamma$ and $H\to\gamma\gamma$.

3 Constraints on the SDM

Apart from the constraints discussed above, namely that we require electroweak symmetry breaking with a vacuum bounded from below and a softly broken $\mathbb{Z}_2$ symmetry, we impose

[2] In our model, just as in the SM, we will have, e.g., $hb\bar{s}$ couplings generated by a loop with two $W^\pm$ bosons with off-diagonal CKM matrix elements.

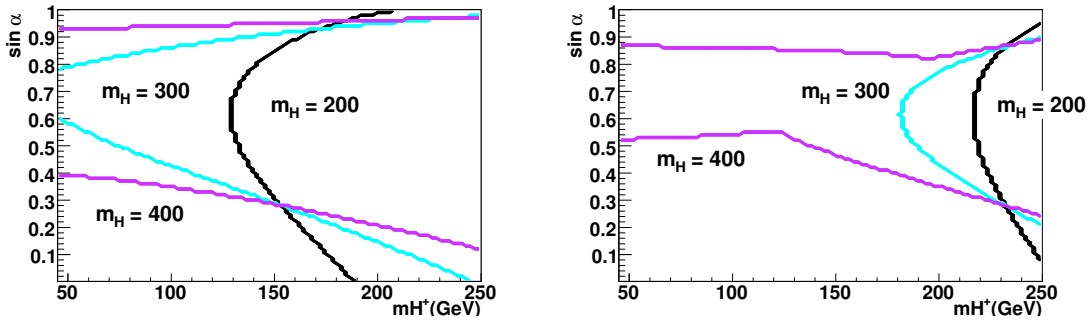

(a) $m_h = 125$ GeV, $m_A = m_{H^\pm}$, $\lambda_3 = 0$.

(b) $m_h = 125$ GeV, $m_A = m_{H^\pm}$, $\lambda_3 = 1$.

Figure 2. Contours displaying allowed regions in parameter space (to the left of/above/below the contour lines), taking into account the theoretical constraints of stability, tree-level unitarity and perturbativity. The black contour displays the allowed region for $m_H = 200$ GeV, cyan $m_H = 300$ GeV and magenta $m_H = 400$ GeV. Here, we have used $\lambda_2 = \lambda_1$ and $\lambda_7 = \lambda_6$, which makes the allowed regions depend only on $|\sin\alpha|$.

several other theoretical and experimental constraints on the model. All of the constraints discussed in this section are included in our numerical work by using the two-Higgs doublet model calculator 2HDMC [34, 35], where we have implemented our model as a special case.

The electroweak vacuum selected by the symmetry breaking mechanism must be stable, which requires that the potential should be bounded from below for any values of the fields. This leads to the conditions (2.9) and three more complicated equations. We also impose the requirements that tree-level scattering of scalars and longitudinal W and Z bosons must be unitary at high energies (the eigenvalues L_i of the S-matrix elements obey $|L_i| \leq 16\pi$) [36–40], and that the quartic scalar couplings are perturbative $|C_{h_i h_j h_k h_\ell}| \leq 4\pi$. We will collectively call these constraints "theoretical constraints". Two examples of the allowed regions in the parameter space of the model are shown, for positive $\sin\alpha$, in figure 2. If we choose $\lambda_2 = \lambda_1$ and $\lambda_7 = \lambda_6$ as the solution to eqs. (2.31) and (2.32), the allowed regions depend only on $|\sin\alpha|$. For other solutions of the $\mathbb{Z}_2$ breaking conditions, the allowed regions depend on the sign of $\sin\alpha$. This is illustrated in figure 3, where we show the allowed regions for different choices of λ_7 (positive) and λ_2. The allowed regions with negative λ_7 values are obtained by mirroring the regions in figure 3 with respect to the $m_{H^\pm}$-axis through $\sin\alpha = 0$.

In general, one could also consider constraints from renormalization group evolution of Yukawa couplings and masses in a similar way as in [12, 41]. Furthermore, one could consider constraints on metastable vacua as in [42, 43]. However, this is beyond the scope of this study.

Any model with new particles that couple to gauge bosons can potentially lead to large contributions to the gauge boson self-energies. Such corrections are constrained by experimental measurements, and can be parametrized by the oblique Peskin–Takeuchi S, T, and U parameters [44], which are defined in terms of contributions to the vacuum po-

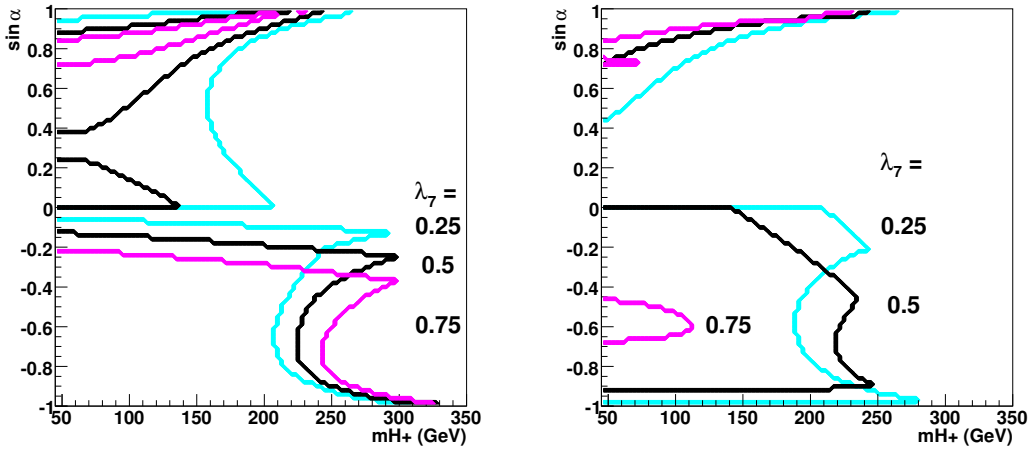

Figure 3. Contours displaying allowed regions in parameter space (to the left of the contour lines), taking into account the theoretical constraints of stability, tree-level unitarity and perturbativity. The cyan contour displays the allowed region for $\lambda_7 = 0.25$, black $\lambda_7 = 0.5$ and magenta $\lambda_7 = 0.75$. In (a) we use $\lambda_2^{(+)}$ from (2.33) and in (b) $\lambda_2^{(-)}$. We have here used $m_h = 125$ GeV, $m_H = 300$ GeV, $m_A = m_{H^\pm}$ and $\lambda_3 = 0$.

larizations of the electroweak gauge bosons. In particular, the T parameter is proportional to the deviation from the SM value of the ρ parameter $\rho = m_W^2/(m_Z^2 \cos^2\theta_W)$. We do not list the explicit expressions here, which are lengthy and involve all scalars. S, T and U do not depend explicitly on the parameters in eq. (2.2) but only implicitly through the scalar masses of the model, equations (2.12), (2.13) and (2.19). Additionally, the mixing angle α only enters as s_α^2 and c_α^2, so S, T and U do not depend on the sign of s_α.

We use 2HDMC to compute the oblique parameters S, T and U and require the obtained values of S and T to fall within the 90% C.L. ellipse of figure 10.7 in [45]. This ellipse is given by values of constant $\mathcal{E}_{\rm ST}(S,T)$, where, approximately,

$$\mathcal{E}_{\rm ST}(S,T) = \left(\frac{\tilde{S}\cos\theta + \tilde{T}\sin\theta}{0.224}\right)^2 + \left(\frac{\tilde{T}\cos\theta - \tilde{S}\sin\theta}{0.068}\right)^2, \tag{3.1}$$

with $\theta = 0.753$, $\tilde{S} = S - 0.051$ and $\tilde{T} = T - 0.077$. In other words, figure 10.7 in [45] shows the $\mathcal{E}_{\rm ST}(S,T) = 1$ ellipse. We use the reference value $m_H^{\rm ref} = 125$ GeV, which is to be compared with the values $115.5 < m_H^{\rm ref} < 127$ GeV used in [45], where U was fixed at $U = 0$, the expected result for models without anomalous gauge couplings. We find that for parameter points in our model with allowed S and T values, we have $0 \lesssim U \lesssim 0.02$.

In figure 4 we show some examples of regions satisfying the experimental constraints on the S and T parameters as well as the theoretical constraints discussed above. We note that in our model, there are two candidates for the new observed Higgs boson, $\mathcal{H}$, with mass $m_{\mathcal{H}} \approx 125$ GeV: either the lightest CP-even scalar h, or the heaviest H. We will in the following refer to the scenario $m_h = 125$ GeV as "Case 1" and to $m_H = 125$ GeV as

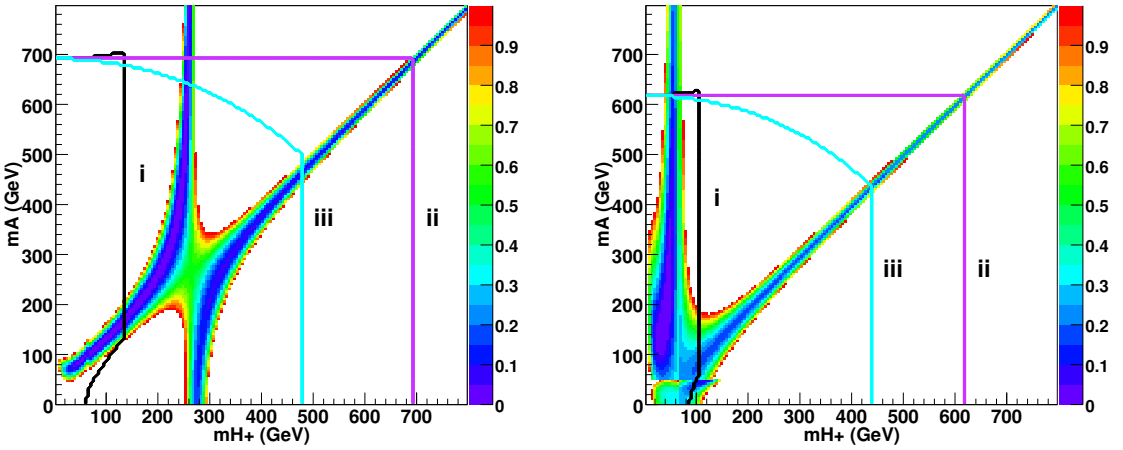

(a) $m_h = 125$ GeV, $m_H = 300$ GeV, $s_\alpha = 0.9$.

(b) $m_h = 75$ GeV, $m_H = 125$ GeV, $s_\alpha = 0.1$.

Figure 4. Some examples of allowed regions in parameter space taking into account theoretical constraints and experimental S and T values. The x-axis shows the charged scalar mass $m_{H^\pm}$ and the y-axis the CP odd scalar mass m_A. The z-axis displays the value of $\mathcal{E}_{\rm ST}(S,T)$ if it fulfills $\mathcal{E}_{\rm ST} \leq 1.0$, see eq. (3.1). The regions to the left of the lines in the figure are the allowed by theoretical constraints for the different values of λ_3 indicated: black (i) $\lambda_3 = 0$, magenta (ii) $\lambda_3 = 2m^2_{H^\pm}/v^2$ and cyan (iii) $\lambda_3 = 4m^2_{H^\pm}/v^2$. Here, we have also used $\lambda_2 = \lambda_1$ and $\lambda_7 = \lambda_6$.

"Case 2". In section 4 we will see that in order to accommodate the experimentally observed signal strengths, $|\sin\alpha|$ must be close to unity in Case 1 and small in Case 2. Motivated by these relationships between $m_{h,H}$ and $\sin\alpha$, we present the constraints in the $(m_{H^\pm}, m_A)$-plane from theory and S and T parameters, using $\sin\alpha = 0.9$ for $m_h = 125$ GeV, and $\sin\alpha = 0.1$ for $m_H = 125$ GeV in figure 4. We use $\lambda_2 = \lambda_1$ and $\lambda_7 = \lambda_6$ in order to satisfy eq. (2.31), see section 2.5. We also present the boundaries for different values of λ_3 (corresponding to the three values $m^2_{22} = 0$ and $m^2_{22} = \pm m^2_{H^\pm}$, according to eq. (2.22)), shown as the regions inside the black, magenta and cyan lines in figure 4. First of all, we see that in order to satisfy the theoretical constraints, the scalar masses can typically not exceed ~ 700 GeV. Secondly, as noted in [46] for 2HDMs, in order to have a small contribution to the S and T parameters, the $H^\pm$ and A masses must satisfy an approximate custodial symmetry (the two branches in the figure). If we define [46]

$$M^2 \equiv m_h^2 \cos^2\alpha + m_H^2 \sin^2\alpha, \tag{3.2}$$

then there is an approximate custodial symmetry if either $m_A \approx m_{H^\pm} + 50$ GeV when $m^2_{H^\pm} \lesssim M^2$, or $m_A \approx m_{H^\pm}$ when $m^2_{H^\pm} \gtrsim M^2$, or $0 \lesssim m_A \lesssim 700$ GeV when $m^2_{H^\pm} \approx M^2$.

In models with charged scalars $H^\pm$, any Feynman diagram that contains a $W^\pm$ also occurs with a $H^\pm$. In particular, this will affect low energy observables such as decay widths of mesons. By considering the effects of $H^\pm$ and A on low energy observables, one can indirectly constrain e.g. $m_{H^\pm}$ for a given set of $C_{H^\pm f\bar{f}'}$ couplings, or in other words ρ^F. For a discussion of the impact of constraints from meson decays on $H^\pm$ in general

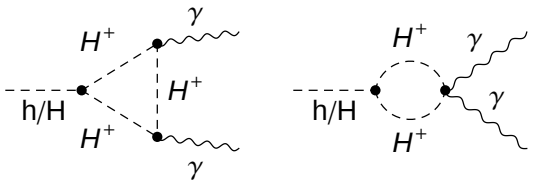

Figure 5. The two additional Feynman diagrams for the process $\mathcal{H} \to \gamma\gamma$ in 2HDMs, $\mathcal{H} = h, H$.

2HDMs we refer to e.g. Ref. [46]. In our model, we will assume that the sizes of the loop-induced couplings between $H^\pm$ and fermions are well below current limits from such flavor observables. In other words, indirect constraints from flavor observables do not apply to the $H^\pm$ and A of our model. The only direct, model independent, constraint prior to LHC that applies to our $H^\pm$ is the measurement of Γ_Z, which gives the limit $m_{H^\pm} > 39.6$ GeV [47].

4 The SDM and the observed Higgs boson at the LHC

In this section, we include collider constraints in our analysis of the SDM parameter space. This is implemented through the 2HDMC interface to HIGGSBOUNDS (version 3.8.0) [48, 49], which includes Higgs searches at LEP, the Tevatron and the LHC (7 TeV data). We do not include all of the very recent LHC results in the present analysis, but this will be discussed further below. Limits on $m_{H^\pm}$ and m_A are not tested with HIGGSBOUNDS, since 2HDMC only calculates tree-level branching ratios for the charged scalar $H^\pm$ and the CP-odd scalar A, see section 5.2 and further below. We will refer to the recently discovered Higgs boson as $\mathcal{H}$ and the SM Higgs boson as $H_{\rm SM}$.

We here mainly consider the $\gamma\gamma$-channel, which is the most significant channel in the discovery of $\mathcal{H}$. Studies of the impact of the $\gamma\gamma$-signal on the IDM has been studied in e.g. [12, 13, 50, 51]. In ref. [52] constraints on general 2HDMs with a softly broken $\mathbb{Z}_2$ symmetry and $\tan\beta \neq 0$ are studied in the light of the new LHC data.

The ATLAS experiment has observed a small excess in the $\gamma\gamma$ signal strength compared to the SM. Here, the signal strength $\mu_{\mathcal{H}\gamma\gamma}$ is defined as

$$\mu_{\mathcal{H}\gamma\gamma} = \frac{\sum_k \sigma_k(pp \to \mathcal{H} + X_k) \times \mathrm{BR}(\mathcal{H} \to \gamma\gamma)}{\sum_k \sigma_k(pp \to H_{\rm SM} + X_k) \times \mathrm{BR}(H_{\rm SM} \to \gamma\gamma)} \ , \tag{4.1}$$

where $\mathcal{H} = h, H$ in our model, and σ_k are the gluon-fusion and vector boson fusion (VBF) hadronic cross sections. The signal strength for other channels, such as $\mu_{\mathcal{H}ZZ}$, are defined in an analogous way. At the time of writing, ATLAS reports the value $\mu_{\mathcal{H}\gamma\gamma} = 1.65 \pm 0.24(\mathrm{stat})^{+0.25}_{-0.18}(\mathrm{syst})$ at a mass $m_{\mathcal{H}} = 126.8 \pm 0.2(\mathrm{stat}) \pm 0.7(\mathrm{syst})$ GeV [4]. The best fit signal strength and mass using all decay channels are $\mu_{\mathcal{H}} = 1.43 \pm 0.16(\mathrm{stat}) \pm 0.14(\mathrm{syst})$ and $m_{\mathcal{H}} = 125.5 \pm 0.2(\mathrm{stat})^{+0.5}_{-0.6}(\mathrm{syst})$ GeV [53]. The CMS experiment does not report any excess in the $\mathcal{H} \to \gamma\gamma$ channel; their best fit value is $\mu_{\mathcal{H}\gamma\gamma} = 0.78 \pm 0.24$ with a best-fit mass of $m_{\mathcal{H}} = 125.4 \pm 0.5(\mathrm{stat}) \pm 0.6(\mathrm{syst})$ GeV [6].

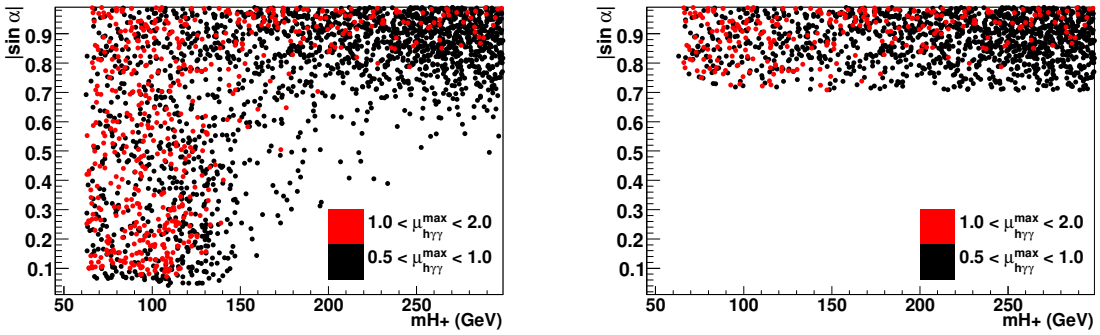

(a) (b)

Figure 6. The maximally obtained $\mu_{h\gamma\gamma} \equiv \mu^{\max}_{h\gamma\gamma}$, with $m_h = 125$ GeV and $m_H = 300$ GeV, for parameters that satisfy all constraints from theory, collider searches with the use of HiggsBounds version 3.8. In (b) the requirement $0.5 < \mu_{hZZ} < 2.0$ is added. We have plotted the points resulting in $1.0 < \mu^{\max}_{h\gamma\gamma} < 2.0$ (red) above the points resulting in $0.5 < \mu^{\max}_{h\gamma\gamma} < 1.0$ (black). The scan is described in the text.

We further consider the $ZZ \to 4\ell$ channel. At the mass $m_{\mathcal{H}} = 124.3^{+0.6}_{-0.5}(\text{stat})^{+0.5}_{-0.3}(\text{syst})$ GeV, ATLAS obtains a best fit signal strength $\mu_{\mathcal{H}ZZ} = 1.7^{+0.5}_{-0.4}$ [5]. The CMS experiment obtains at $m_{\mathcal{H}} = 125.7$ GeV the signal strength $\mu_{\mathcal{H}ZZ} = 0.92 \pm 0.28$ [7]. In the following, we will consider signal strengths $0.5 < \mu_{\mathcal{H}\gamma\gamma}, \mu_{\mathcal{H}ZZ} < 2.0$ (where $\mathcal{H} = h, H$) to be compatible with observation.

In our model, the signal strength $\mu_{\mathcal{H}\,\gamma\gamma}$ becomes

$$\mu_{h\gamma\gamma} = \sin^2\alpha\,\frac{\text{BR}(h \to \gamma\gamma)}{\text{BR}(H_{\text{SM}} \to \gamma\gamma)}\,, \quad \mu_{H\gamma\gamma} = \cos^2\alpha\,\frac{\text{BR}(H \to \gamma\gamma)}{\text{BR}(H_{\text{SM}} \to \gamma\gamma)}\,, \tag{4.2}$$

since h couples as $\sin\alpha$ both to quarks in the gg-fusion process and to vector boson pairs in VBF, whereas H couples as $\cos\alpha$.

The matrix element for $\mathcal{H} \to \gamma\gamma$ at lowest order in 2HDMs, and in particular in our model, has contributions from two additional Feynman diagrams compared to the SM, with a pair of charged scalars in the loop, as shown in figure 5. These two diagrams contain the couplings between $\mathcal{H}$ and H^+H^-

$$g_{hH^+H^-} = -\mathrm{i}v\,(-\lambda_3 \sin\alpha + \lambda_7 \cos\alpha)\,, \quad g_{HH^+H^-} = -\mathrm{i}v\,(\lambda_3 \cos\alpha + \lambda_7 \sin\alpha) \tag{4.3}$$

in the matrix element for the partial width $\Gamma_{\mathcal{H}\to\gamma\gamma}$. The inclusion of the charged scalars in the loop can enhance the $\Gamma_{\mathcal{H}\to\gamma\gamma}$ and $\text{BR}(\mathcal{H} \to \gamma\gamma)$ compared to the SM and therefore also $\mu_{\mathcal{H}\gamma\gamma}$.

In order to deduce the regions of parameter space in our model that are compatible with the experimentally observed $\gamma\gamma$ and ZZ signal strengths and that satisfy constraints from EWPT, theory and limits from previous collider experiments (through HiggsBounds), we scan in the $(m_{H^\pm}, \sin\alpha)$-plane over the λ_3 and λ_7 parameters. For a given λ_7 all solutions to equations (2.31) and (2.32), i.e. λ_2 values according to equation (2.33), are tested. The

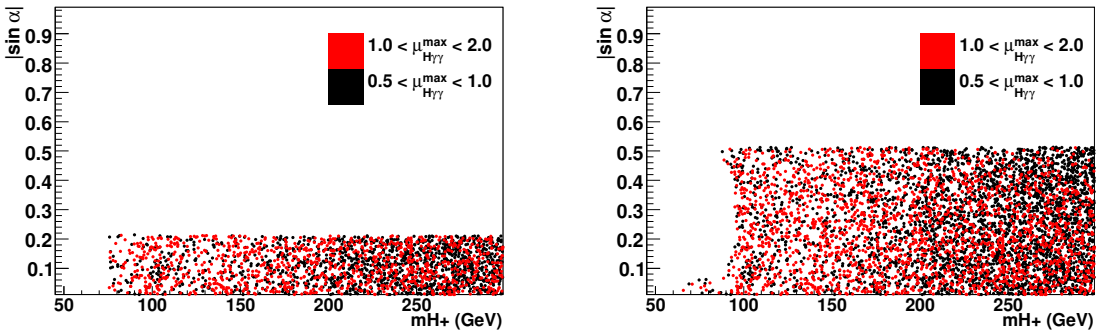

(a) $m_h = 75$ GeV and $m_H = 125$ GeV.

(b) $m_h = 95$ GeV and $m_H = 125$ GeV.

Figure 7. The maximally obtained $\mu_{H\gamma\gamma} \equiv \mu^{\max}_{H\gamma\gamma}$, for parameters that satisfy all constraints from theory, collider searches with the use of HiggsBounds version 3.8 and the requirement $0.5 < \mu_{HZZ} < 2.0$. We have plotted the points resulting in $1.0 < \mu^{\max}_{H\gamma\gamma} < 2.0$ (red) above the points resulting in $0.5 < \mu^{\max}_{H\gamma\gamma} < 1.0$ (black). The scan is described in the text.

scan proceeds by sampling uniformly from the following intervals:

$$m_{H^\pm} \in [45, 300]\,\text{GeV}\,, \quad |\sin\alpha| \in [0, 1]\,, \quad \lambda_3 \in [-5, 15]\,, \quad \lambda_7 \in [-10, 10]. \tag{4.4}$$

We need only consider $|\sin\alpha|$ since it can be shown that the allowed points are independent on the sign of $\sin\alpha$.

In Case 1, m_A is taken as $m_A = m_{H^\pm} + 50$ GeV in order to fulfill the constraints from EWPT. In Case 1 we also use $m_H = 300$ GeV. In Case 2 we use $m_h = 75$ or 95 GeV with $m_A = m_{H^\pm}$ to fulfill EWPT constraints. The maximum signal strengths $\mu^{\max}_{\mathcal{H}\gamma\gamma}$ for parameter points that satisfy all the constraints are shown in figures 6 and 7 for the two cases respectively.

In total, we generate 5×10^4 points for each (m_h, m_H) configuration. In Case 1, 1432 points pass all constraints and give $0.5 < \mu^{\max}_{h\gamma\gamma} < 1.0$ and 286 points give $1.0 < \mu^{\max}_{h\gamma\gamma} < 2.0$. In Case 2 with $m_h = 75$ (95) GeV, 1466 (3385) points pass all constraints and give $0.5 < \mu^{\max}_{H\gamma\gamma} < 1.0$, and 1130 (2247) points give $1.0 < \mu^{\max}_{H\gamma\gamma} < 2.0$.

We find an allowed region for Case 1 compatible with observed signal strengths, such that $0.7 \lesssim |\sin\alpha|$. There is also a region $m_h/2 \lesssim m_{H^\pm} \lesssim 150$ GeV, where the $\gamma\gamma$ signal strength is compatible with observations. However, for such low values of $|\sin\alpha|$, the signal strength for $h \to ZZ$ is not compatible with data. (The $h \to ZZ$ signal strength scales as $\sin^2\alpha$ in Case 1 as long as the decay channels into other scalars can be neglected). One should therefore consider $|\sin\alpha| \approx 0.7$ as a lower limit for the allowed parameter space. There is also an allowed region with $m_{H^\pm} < m_h/2$ for $0.8 \lesssim |\sin\alpha|$. This region is not shown in figure 6 since it is a very finely tuned region and can only be seen if one generates more points according to (4.4). This region exists because the coupling $g_{hH^+H^-}$ can be made small enough to make $\text{BR}(h \to H^+H^-)$ negligible. For such low $m_{H^\pm}$ one might think that the LEP constraints on $m_{H^\pm}$ are violated (see section 5.2.4). However, the majority of

the allowed points compatible with $\mu_{h\gamma\gamma}$ for $m_{H^\pm} < m_h/2$ have $\mathrm{BR}(H^\pm \to W^\pm\gamma) > 99\%$ which we have assumed avoids the LEP constraints. We refer the reader to section 5.2 for details concerning the $H^\pm$ decays in our model.

For Case 2, with $m_h = 75$ GeV or $m_h = 95$ GeV, the preferred regions are $|\sin\alpha| \lesssim 0.2$ or $|\sin\alpha| \lesssim 0.5$ respectively, both with with $m_h \lesssim m_{H^\pm}$, see figure 7. For $m_h = 95$ GeV, an allowed region with $|\sin\alpha| \lesssim 0.1$ and $m_H/2 \lesssim m_{H^\pm} \lesssim m_h$ exists with relatively high statistics. Analogous to the previously discussed Case 1, there is also an allowed region, with $m_{H^\pm} < m_H/2$ and $|\sin\alpha| \lesssim 0.2$ in Case 2, which is not shown in figure 7 due to low statistics.

We have not considered the off-shell decay channels $\mathcal{H} \to H^{+(*)}H^{-*}$ nor $A^{(*)}A^*$, which are not included in the 2HDMC code. However, due to the smallness of $\Gamma_{H^\pm}$ and Γ_A, they are not important (see sections 5.2.4 and 5.3.2).

In Case 1, we note that a conservative lower limit on m_H can be obtained by using the searches for the SM Higgs boson by the ATLAS and CMS experiments. As an example we consider figure 12a of Ref. [5] from ATLAS. This figure shows $\sigma(gg \to H_{\mathrm{SM}}) \times \mathrm{BR}(H_{\mathrm{SM}} \to ZZ) \times \mathrm{BR}(ZZ \to 4\ell)$ as a function of $m_{H_{\mathrm{SM}}}$. Assuming no other decay modes of the H boson of our model than into SM particles, we should rescale their result with $\cos^2\alpha$ in order to compare with our model. For $\sin\alpha = 0.9$, our predicted cross section is below the present exclusion limit for $m_H > 200$ GeV. For $\sin\alpha = 0.8$ we are within and below the 1σ exclusion limit when $m_H \gtrsim 300$ GeV, still assuming no other decay modes of the H boson than into SM particles. If decay modes that involve any of the new scalars in our model are open, in particular the hh mode but possibly also the $H^\pm W^\mp$ and AZ modes, then lower m_H and $\sin\alpha$ values are not excluded. It would be interesting to further analyze our model in the light of the very recent LHC results, e.g. by using the updated HiggsBounds [54, 55] and the new code HiggsSignals [56].

5 Decays of the Scalars in the SDM

In this section we present the decay branching ratios and widths for the scalars in our model. We first briefly discuss the decays of the CP-even bosons h and H followed by a longer discussion of the decays of the charged scalar $H^\pm$. Some of the discussion regarding technical details of the $H^\pm$ decays is relegated to Appendices B and C. We then finish this section by briefly discussing the decays of the A bosons, which are computed analogously to the $H^\pm$ decays.

5.1 Decays of the non SM-like CP even scalar h or H

The decay modes of the h and H bosons are as in a Type-I 2HDM with $\tan\beta = 0$. In this section, we will focus on Case 1 and Case 2, which were discussed in section 4. For the calculations of the branching ratios of h and H, we use 2HDMC.

We first consider Case 1, where $m_h = 125$ GeV. The decay modes of h must be SM-like in order to reproduce the recent LHC results. This constrains the masses of the charged scalar $H^\pm$ and the CP-odd A to be large enough to prohibit e.g. $h \to H^+H^-$ and $h \to AA$, unless the couplings are small as discussed in section 4. The heavier H boson, which can

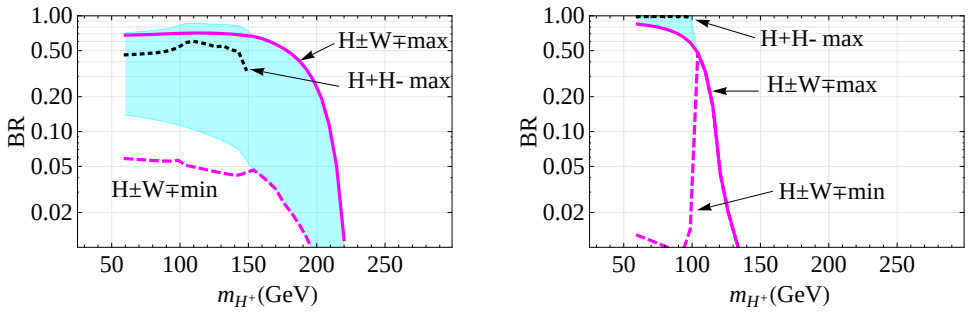

Figure 8. The branching ratios of the H boson as a function of $m_{H^\pm}$ when scanning over λ_3 and λ_7 (see the text for details) for $m_H = 300$ GeV (left) and $m_H = 200$ GeV (right): maximal BR($H \to H^+H^-$) is shown as a black dotted line, whereas BR($H \to H^\pm W^\mp$)$^{\max}$ and BR($H \to H^\pm W^\mp$)$^{\min}$ are shown as solid and dashed magenta lines. The cyan band shows the sum BR($H \to H^\pm X$).

be as light as ~ 200 GeV according to the discussion in section 4, can decay into $H^\pm W^\mp$, H^+H^-, AA and AZ if any of these channels are open. In this case they will be potential production channels for charged scalars and CP-odd scalars.

In order to investigate these decays in more detail, we have performed a scan in the (λ_3, λ_7)-plane according to

$$-5 \leq \lambda_3 \leq 15\,, \qquad -10 \leq \lambda_7 \leq \min\{10\,,\, \lambda_7^{\max}\}\,, \tag{5.1}$$

in steps of 50 each in λ_3 and λ_7 for a given $(m_{H^\pm}, \sin\alpha)$ point, where $\lambda_7^{\max}$ is given by eq. (2.36), using $\sin\alpha = 0.9$, $m_h = 125$ GeV and $m_A = m_{H^\pm} + 50$ GeV as well as imposing the theoretical constraints and $0.5 < \mu_{h\gamma\gamma} < 2.0$ and $0.5 < \mu_{hZZ} < 2.0$. The results are summarized in figure 8a and figure 8b for $m_H = 300$ and 200 GeV, respectively. From figure 8a we see that for $m_H = 300$ GeV the branching ratio of the H scalar into a pair of charged scalars H^+H^- can be as large as 60% and $H \to H^\pm W^\mp$ can be up to 70%. Looking at the sum of the two, we see that the branching ratio for $H \to H^\pm X$ is substantial for $m_{H^\pm} \lesssim 150$ GeV. Turning to the case $m_H = 200$ GeV shown in figure 8b we see that the decay $H \to H^+H^-$ can dominate completely whereas $H \to H^\pm W^\mp$ is substantial for $m_{H^\pm} \lesssim 120$ GeV.

In Case 2, the possible decays modes of H are the same as in Case 1. However, in order to accommodate the recent LHC results, the signal strengths must be very SM-like and therefore puts limits on $m_{H^\pm}$ and m_A. The branching ratios of h in Case 2 should then also be SM-like since no other decay channels are open.

5.2 Decays of the charged scalar $H^\pm$

We now turn to the decay of the charged scalar $H^\pm$. The main issue here is that below the $H^\pm \to W^\pm S$ threshold, where S is the lightest of the neutral scalars, it is not known *a priori* which is the largest of the partial decay widths: $H^\pm \to f\bar{f}'$, $H^\pm \to W^\pm Z/\gamma$ (which

proceeds at one-loop level at lowest order) or $H^\pm \to W^{\pm *} S^* \to 4$ or 6 fermions (which are tree level processes, suppressed by massive propagators and multi-particle phase-space).

All loop calculations of the $H^\pm$ and A decays in this paper have been performed by implementing the model in the FeynArts [57] and FormCalc [58, 59] packages with the help of the FeynRules package [60].[3] The calculations have been performed in Feynman–'t Hooft gauge, i.e. R_ξ gauge with $\xi = 1$, and renormalization conditions and counterterms have been implemented in FormCalc directly as this is not included in models generated using FeynRules. Details of the calculations are given in the rest of this section, and details of the renormalization and the chosen on-shell renormalization scheme are given in Appendix B.

5.2.1 $H^\pm \to f\bar{f}'$

Due to the assigned $\mathbb{Z}_2$ parities of the $\Phi_{1,2}$ fields and the fermions, the charged scalar, which resides solely in Φ_2, does not couple to fermions at tree level. Since the CP-even mass eigenstates are a mixture of the neutral and real components from Φ_1 and Φ_2 it is possible for the charged scalar to interact with fermions through the terms $m_{12}^2 \Phi_1^\dagger \Phi_2 + \text{h.c.}$ in the scalar potential. Because of the mixing, the amplitudes for all such diagrams will be proportional to $\sin 2\alpha \propto |m_{12}|$ (see eqs. (2.8) and (2.26)).

[3] The FeynRules model can be obtained from the authors.

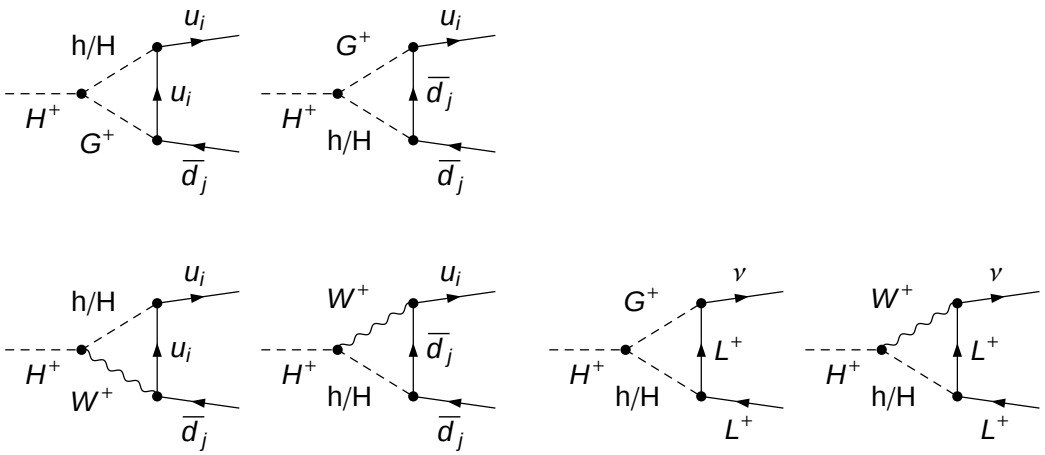

Figure 9. Feynman diagrams in R_ξ gauge for the effective vertex for (a): $H^+ \to u_i \bar{d}_j$ and (b): $H^+ \to L^+ \nu$. Here, u_i and d_i denote up- and down-type quarks of family i. L^+ denotes a positively charged lepton; e^+, μ^+, τ^+ and ν the corresponding neutrino. Diagrams that contain propagators denoted by h/H are to be counted as two diagrams: one with a h boson running in the loop and one with a H boson instead. The effective vertices for $Au_i\bar{u}_i$ and AL^+L^- are described at one-loop order by the same set of diagrams as in (a) and (b) but with the replacements $A \to H^+$, $W^+ \to Z$, $G^+ \to G^0$, $\bar{d}_i \to \bar{u}_i$ and $\nu \to L^-$.

There are several different ways for the charged scalar to couple to two fermions. We start by considering the effective vertex generated by the Feynman diagrams shown in figure 9, and given in eq. (C.2) in appendix C. Since the coupling $C_{H^\pm f\bar{f}'} \sim \rho^F$ is absent at tree level and no counterterm is obtained by performing field and coupling expansions in $\mathcal{L}_{\text{Yukawa}}$, the loop-generated coupling is UV finite. This has also been verified explicitly using the FeynArts and FormCalc implementation.

Another contribution to the matrix element $\mathcal{M}_{H^\pm \to f\bar{f}'}$ comes from mixing of the charged scalar with the longitudinal component of the $W^\pm$ boson or the charged Goldstone boson $G^\pm$ since we are using R_ξ gauge. This contribution also arises due to the $m_{12}^2\Phi_1^\dagger\Phi_2$ + h.c. term in the scalar potential. Feynman diagrams for the $H^\pm W^\mp$ and $H^\pm G^\mp$ mixing contribution to $H^\pm \to f\bar{f}'$ are shown in figures 10 and 11.

In the present work, we follow the procedure for renormalization described in [61], which means that no tadpole diagrams contribute and the real parts of the $H^\pm W^\mp$ and $H^\pm G^\mp$ mixings are absent for on-shell charged scalars. Again we refer to Appendix B for details. Below the $hW^\pm$ threshold, only the vertex-diagrams in figure 9 contribute to $\Gamma_{H^\pm \to f\bar{f}'}$ in the present renormalization scheme. As a consequence, for charged scalar masses below $m_h + m_W$, the width for $H^\pm \to f\bar{f}'$ is proportional to the fermion mass m_f and vanishes when $m_f \to 0$. Above the $m_h + m_W$ threshold, where the $H^\pm W^\mp$-mixing diagrams develops a non-zero imaginary part (which is unaffected by the renormalization scheme, see figure 24), the width will not vanish in the limit $m_f \to 0$. We have also verified, with our FeynArts and FormCalc implementation, that the final expression for the partial width $\Gamma_{H^\pm \to f\bar{f}'}$, including all contributions, is indeed UV finite.

Finally we want to emphasize that the $H^\pm \to f\bar{f}'$ partial width is proportional to $\sin^2 2\alpha$ and does not depend on the parameters λ_2, λ_3 or λ_7. In our numerical calculations we include QCD radiative corrections for final state quarks up to order α_s^2, according to eq. (14) in [34], which is based on [62–64]. We will also in the following discussion set V_{CKM} equal to the unit matrix.

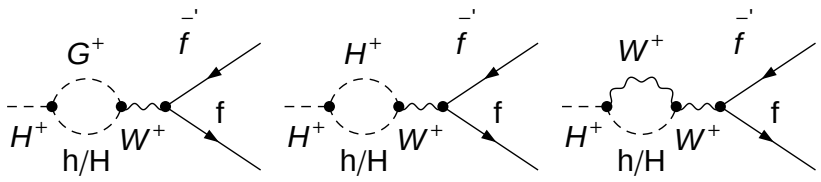

Figure 10. H^+W^- mixing contribution to $H^+ \to f\bar{f}'$. The same set of diagrams exists for the AZ mixing contribution to $A \to f\bar{f}$ with the replacements $A \to H^+$, $W^+ \to Z$, $G^+ \to G^0$ and $\bar{f}' \to \bar{f}$. There is also the possibility to draw diagrams where the A boson mixes with a h/H boson which in turn go into a pair of fermions, but all such diagrams vanish due to CP conservation in the scalar sector. Diagrams that contain propagators denoted by h/H are to be counted as two diagrams: one with a h boson running in the loop and one with a H boson instead.

In figure 12, the partial widths $\Gamma_{H^\pm\to\tau\nu}$ and $\Gamma_{H^\pm\to cs}$ are shown. The widths are very small, less than ~ 1 eV. This is partially due to the small Yukawa couplings m_s/v, m_c/v and m_τ/v, on which all diagrams below the $hW^\pm$ threshold depend through the $H_i\bar{f}f$ vertex, $H_i = h, H$. Above the $hW^\pm$ threshold, the diagrams in figure 10, which are independent of the Yukawa couplings, start to contribute according to the chosen renormalization scheme. The smallness of the widths is also due to the loop suppression. In section 5.3.1, we compare the partial width for the process $A \to \tau^+\tau^-$ (which is analogous to $H^\pm \to \tau\nu$) evaluated in our model and in a generic 2HDM in order to extract the size of the loop suppression. We also note that the widths depend on m_h and m_H since diagrams with h and H propagators interfere destructively. Furthermore, the $\tau\nu$ and cs widths are similar in size due to the scaling with the fermion masses in the $H_i\bar{f}f$ vertex.

5.2.2 $H^\pm \to W^\pm Z/\gamma$

We now discuss the decay channels $H^\pm \to W^\pm Z/\gamma$, starting with $H^\pm \to W^\pm\gamma$. Since the electromagnetic current j^μ_{EM} must be conserved classically, only couplings between photons and particle–antiparticle pairs exist at tree level. This means in particular that the coupling $H^\pm W^\mp\gamma$ is absent, irrespective of the underlying model giving rise to the charged scalar $H^\pm$ state. However, this coupling can in general be generated at higher orders. The Feynman diagrams that contribute to the amplitude at one-loop order in R_ξ gauge are shown in figure 13.

In principle, the diagrams in figure 14 could also contribute to longitudinally polarized $W^\pm$ bosons, $W^\pm_L$, but in fact all vanish. This can be understood by the form of the $H^+H^-\gamma$

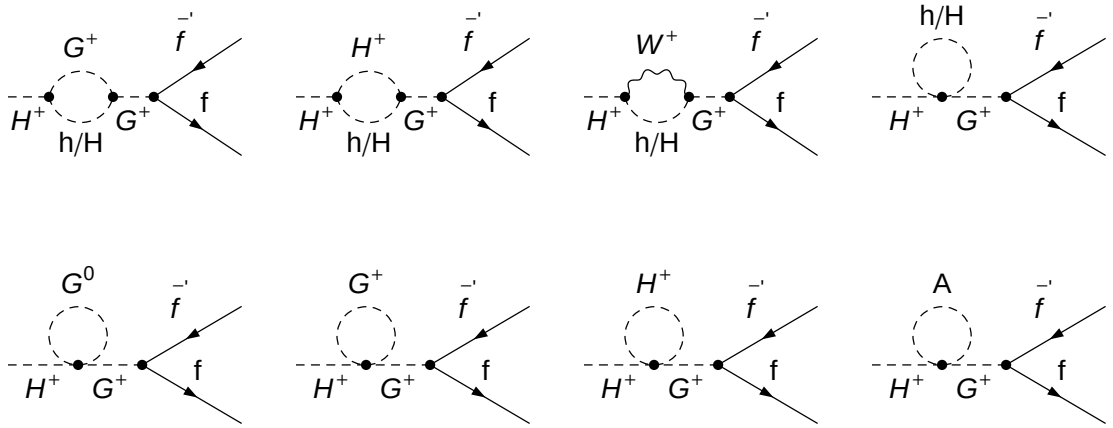

Figure 11. H^+G^- mixing contribution to $H^+ \to f\bar{f}'$. The last five diagrams are purely real and vanish in on-shell renormalization schemes [61]. The same set of diagrams exists for the AG^0 mixing contribution to $A \to f\bar{f}$ with the replacements $A \to H^+$, $W^+ \to Z$, $G^+ \to G^0$ and $\bar{f}' \to \bar{f}$.

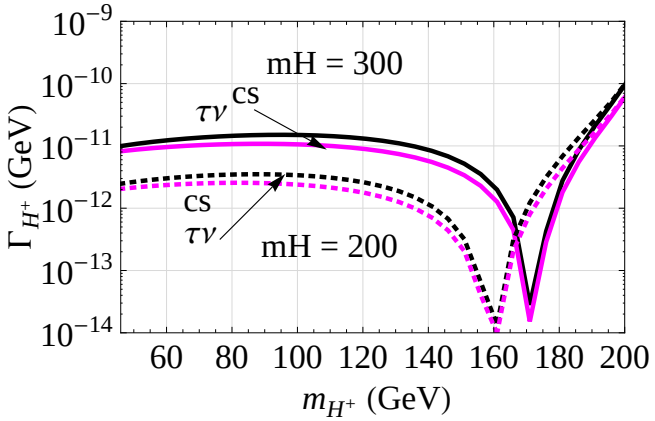

Figure 12. The partial widths $\Gamma_{H^\pm\to\tau\nu}$ (black) and $\Gamma_{H^\pm\to cs}$ (magenta) evaluated for $m_h = 125$ GeV, $\sin\alpha = 0.9$. For the solid lines we have $m_H = 300$ GeV, and for the dotted lines $m_H = 200$ GeV.

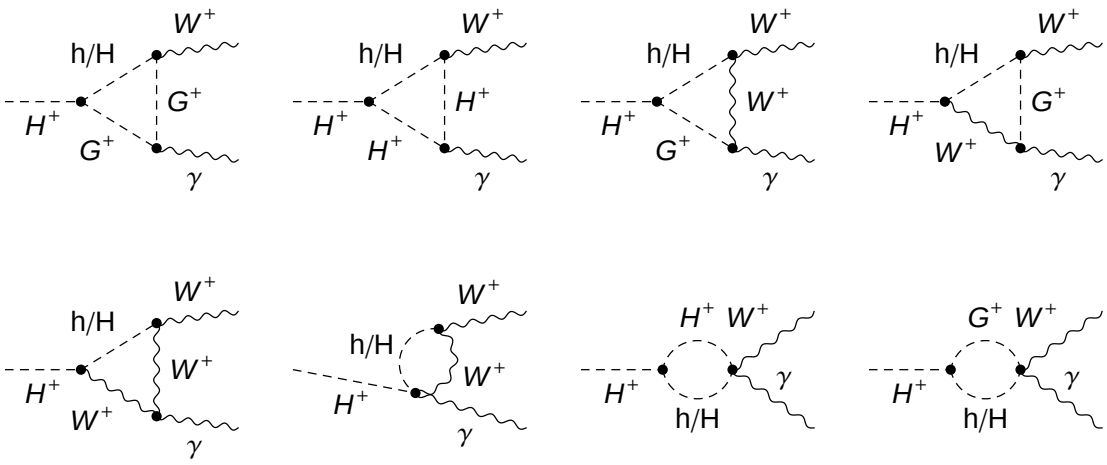

Figure 13. Feynman diagrams in R_ξ gauge for the $H^\pm W^\mp\gamma$ effective vertex at one-loop order. Diagrams that contain propagators denoted by h/H are to be counted as two diagrams: one with a h boson running in the loop and one with a H boson instead.

coupling, for which the Feynman rule reads

$$H^+H^-\gamma \;:\quad \mathrm{ie}\left[p^\mu_{H^+} - p^\mu_{H^-}\right], \tag{5.2}$$

where the four momenta are taken to be incoming. Due to four momentum conservation at each vertex, we obtain $p^\mu_{H^+\mathrm{ext.}} - p^\mu_\gamma = p^\mu_{H^+\mathrm{int.}} = p^\mu_W$ (at the $H^+H^-\gamma$ vertex in the diagrams in figure 14), which contracted with the final state polarization vector ϵ_μ for the $W^\pm$ boson gives

$$p^\mu_W\,\epsilon_\mu(\sigma, p_W) = 0, \tag{5.3}$$

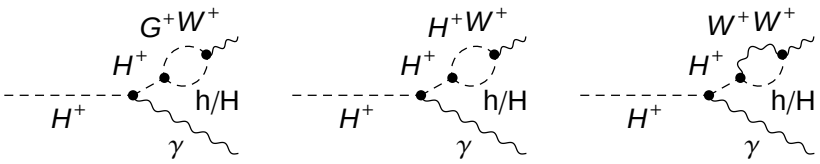

Figure 14. Feynman diagrams in R_ξ gauge that contribute to the process $H^\pm \to W^\mp\gamma$ at one-loop level, where the external $W^\pm$ boson has longitudinal polarization, $W_L^\mp$. Diagrams that contain propagators denoted by h/H are to be counted as two diagrams: one with a h boson running in the loop and one with a H boson instead. All of these diagrams vanish due to the form of the $H^+H^-\gamma$ vertex, as explained in the text.

according to the gauge condition for massive spin-1 bosons, for all polarizations σ. This demonstrates that all the diagrams in figure 14 vanish and has also been verified with our FormCalc implementation.

Similarly, the diagrams in figure 17, which are a subset of possible diagrams for the matrix element of $H^\pm \to W^\pm Z_L$, vanish by the same argument applied to the $AH^\pm W^\mp$ coupling,

$$AH^\pm W^\mp \; : \quad g_{AH^\pm W^\mp} \left[p^\mu_{H^\pm} - p^\mu_A\right], \tag{5.4}$$

where the four-momenta are taken to be incoming. It is important that the contributions from AZ-mixing vanish at one-loop level in $H^\pm$ decays. If they did not, then we would not have a consistent renormalization scheme (see Appendix B).

One should also add to the matrix element $\mathcal{M}_{H^\pm\to W^\pm\gamma}$ all the diagrams from the $H^\pm W^\mp$ and $H^\pm G^\mp$ mixing previously discussed for the $H^\pm \to f\bar{f}'$ processes, by substituting $W^+\gamma$ for $f\bar{f}'$ in the diagrams depicted in the figures 10 and 11. We do not include diagrams with external Goldstone bosons in the processes $H^\pm \to W^\pm Z/\gamma$ since we employ the standard unitary gauge prescription for summing over the physical polarization states of the final state $W^\pm$ and Z bosons,

$$\sum_\sigma \epsilon^*_\mu(\sigma,p)\,\epsilon_\nu(\sigma,p) = -g_{\mu\nu} + \frac{p_\mu p_\nu}{m_V^2}, \tag{5.5}$$

where $V = W^\pm$ or Z.

Before continuing with further $H^\pm$ decays, we now want to briefly compare the decay modes calculated so far. Above the on-shell threshold $m_{H^\pm} > m_W$ we find that $H^\pm \to W^\pm\gamma$ naturally dominates over $H^+ \to \tau^+\nu_\tau \,/\, c\bar{s}$ by several orders of magnitude, as illustrated in figure 15. (However, as will be discussed below, it is possible to tune the parameters to make $H^\pm \to W^\pm\gamma$ become very small.) The reason for this can be found in the different couplings appearing in the respective loop diagrams. As was discussed in the previous section, all the diagrams that contribute to $\Gamma_{H^\pm\to f\bar{f}'}$ are proportional to the small Yukawa couplings for $m_{H^\pm} < m_h + m_W$. Above the threshold this partial amplitude is more or less unchanged. In contrast, the leading order diagrams that contribute to $H^\pm \to W^\pm\gamma$ do not depend on the

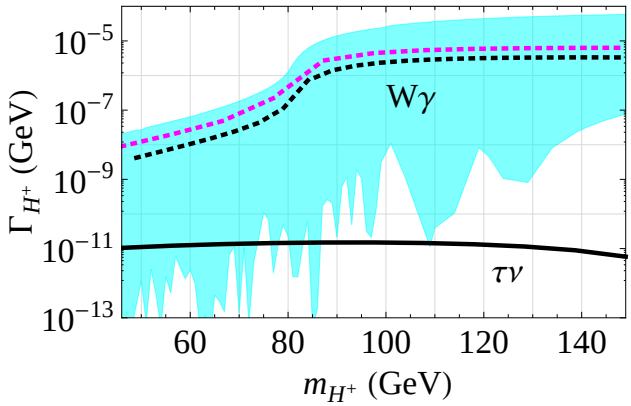

Figure 15. The cyan band shows the maximal and minimal obtained $\Gamma_{H^\pm \to W\gamma}$ by scanning according to eq. (5.1). The dotted magenta line shows $\Gamma_{H^\pm \to W\gamma}$ and the solid black shows $\Gamma_{H^\pm \to \tau\nu}$, evaluated at $\lambda_3 = 2(m_{H^\pm}/v)^2$ and $\lambda_7 = \lambda_6$. The dotted black line shows $\Gamma_{H^\pm \to W\gamma}$ evaluated at $\lambda_3 = \lambda_7 = 0$ which makes the contribution from diagrams containing $H_i H^+ H^-$ vertices ($H_i = h, H$) vanish according to (4.3).

Yukawa couplings, and thus $H^\pm \to W^\pm\gamma$ dominates over $H^+ \to \tau^+\nu_\tau \,/\, c\bar{s}$. The situation is similar to the case in the Standard Model where $H_{\rm SM} \to W^+W^-$ dominates over the $b\bar{b}$ channel if it is open. It is well known that by including the width of the $W^\pm$ bosons, i.e. $H_{\rm SM} \to W^{+*}W^{-*} \to$ fermions, the $W^{+*}W^{-*}$ decay mode of the $H_{\rm SM}$ dominates over $b\bar{b}$ far below the threshold; $m_{H_{\rm SM}} < 2m_W$. As we will now show, the situation is similar in our model, i.e. the $H^\pm \to W^{\pm *}\gamma$ mode dominates over the $H^\pm \to f\bar{f}'$ modes even for charged scalar masses $m_{H^\pm} < m_W$.

To investigate this, we include the effect of subsequent decays of the $W^\pm$ boson, by considering the process $H^\pm \to W^{\pm *}\gamma$, using the method of "smeared mass unstable particles" [65, 66] described in Appendix D. Formally, one should consider all contributions to the process $H^\pm \to f\bar{f}'\gamma$, with a photon energetic enough to be detected. The diagrams contributing to this process would be the same as those for $H^\pm \to f\bar{f}'$ with an external photon radiated off any charged particle. We do not do this here, since to be consistent, we would then also have to include all other $\mathcal{O}(\alpha_{\rm EM})$ corrections to those widths, which are needed to cancel IR divergences. This procedure will then require two-loop calculations, a cumbersome task that will not alter the overall result regarding our $H^\pm \to W^{\pm *}\gamma \to f\bar{f}'\gamma$ calculation.

The result of the inclusion of the width of the $W^\pm$ boson is that, due to its broadness and the smallness of $\Gamma_{H^\pm \to \tau\nu}$ and $\Gamma_{H^\pm \to cs}$, the process $H^\pm \to W^{\pm *}\gamma$ clearly dominates the spectrum even below the threshold for $H^\pm \to W^\pm\gamma$, as shown in figure 18 below and in figure 15 above.

The $H^\pm \to W^\pm Z/\gamma$ widths are proportional to $\sin^2 2\alpha$ and are independent of λ_2. They do however depend on the λ_3 and λ_7 parameters through the H^+H^-h and H^+H^-H vertices present in the second and seventh diagram in figure 13. In figure 15 we give the

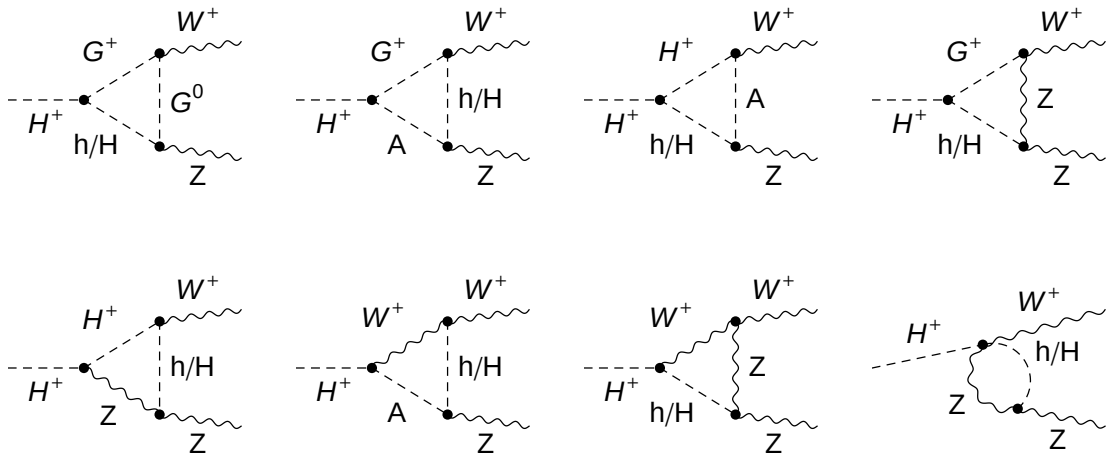

Figure 16. Feynman diagrams in R_ξ gauge that contribute to the process $H^\pm \to W^\mp Z$ at one-loop level. Diagrams that contain propagators denoted by h/H are to be counted as two diagrams: one diagram with a h boson running in the loop and one with a H boson instead.

partial decay width $H^\pm \to W^\pm\gamma$ for the canonical choice of $\lambda_3 = 2(m_{H^\pm}/v)^2$ with $\lambda_7 = \lambda_6$ as well as when scanning over λ_3 and λ_7 according to eq. (5.1). The conclusion is that for the vast majority of parameter space, the $W\gamma$ mode dominates over the $\tau\nu$ and cs modes. We note that it seems possible to tune the parameters λ_3 and λ_7 for a given $m_{H^\pm}$ to give a very small $\Gamma_{H^\pm\to W^\pm\gamma}$. This is most likely due to cancellations between the diagrams containing $H_iH^+H^-$ vertices, $H_i = h, H$ (which depend on λ_3 and λ_7, see eq. (4.3)) with diagrams containing $H_iH^\pm W^\mp$ vertices (which depend on gauge couplings, see appendix A). However, we do not analyze this further here.

We now turn to the process $H^\pm \to W^\pm Z$. The tree-level coupling $g_{H^\pm W^\mp Z}$ depends on the $\mathrm{SU}(2)_L$ and Y representations of the different scalar multiplets in a given model, and their vevs. In models where only $\mathrm{SU}(2)_L$ doublet representations are present, the coupling $g_{H^\pm W^\mp Z}$ vanishes at tree level. This coupling can in general be generated at higher orders. The diagrams for the process $H^\pm \to W^\mp Z$ at one-loop order are the same diagrams as for $H^\pm \to W^\mp\gamma$ (replace $\gamma \to Z$) plus the diagrams in figure 16.

At this stage, we do not include off-shell effects in the $H^\pm \to W^\pm Z$ decays. The reason will become clear below in section 5.2.4 where we will see that since $m_h = 125$ GeV or lighter, the tree level decay $H^\pm \to W^{\pm(*)}h^{(*)}$ will dominate over $H^\pm \to W^\pm Z$ as soon as h can be produced on-shell in $H^\pm \to W^{\pm *}h$. Now, since $m_h = 125$ GeV is below the $W^\pm Z$ threshold, this will always be true. The inclusion of $H^\pm \to W^{\pm *}Z^*$ does not alter this result. However, it can in principle influence the importance of the $H^\pm \to W^\pm\gamma$ mode below the WZ threshold, as indicated in figure 18. In addition, the inclusion of off-shell top quarks could also be important when we consider which decay mode is sub-dominant (at the percentage level). We leave these questions for future studies.

Finally, we have checked, using the FeynArts and FormCalc implementation of our

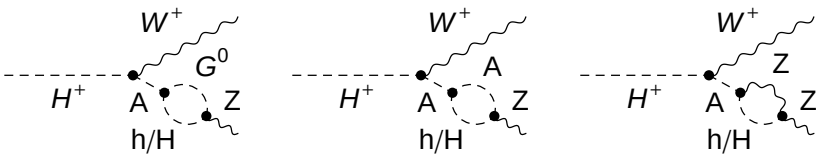

Figure 17. Feynman diagrams in R_ξ gauge that contribute to the process $H^\pm \to W^\mp Z$ at one-loop level, where the external Z boson has longitudinal polarization, Z_L. There is also the possibility to draw diagrams, with a $H^\pm W^\mp h/H$ vertex, where h/H goes into an external Z boson. Those diagrams vanish due to the different quantum numbers of h/H and Z. Diagrams that contain propagators denoted by h/H are to be counted as two diagrams: one diagram with a h boson running in the loop and one with a H boson instead. All of the diagrams in this figure vanish due to the form of the $AH^\pm W^\mp$ vertex as discussed in the text.

model, that the calculated partial widths of $\Gamma_{H^\pm \to W^\pm Z/\gamma}$ are UV finite. For completeness we also note that the processes $H^\pm \to W^\pm Z/\gamma$ have been considered for the MSSM, as well as type I and II 2HDMs, in [61].

5.2.3 $H^\pm \to W^\pm h/H/A \to$ multiple fermions

In addition to the loop-decays already discussed, the $H^\pm$ can also decay into fermions via, possibly off-shell $W^\pm, h, H$ and A bosons. Here we limit the discussion to decays into 4 or 6 fermions, $\Gamma_{H^\pm \to 4f/6f}$. For 4 fermion decays the only relevant channel is

$$\Gamma_{H^\pm \to 4f} = \Gamma(H^\pm \to [W^{\pm *} \to 2f] + [h^*/H^* \to b\bar{b}]). \tag{5.6}$$

For 6 fermion final states there are several different amplitudes that contribute. In principle the partial width should be calculated from the sum of all of all these. In line with this we add the contributions from (possibly) virtual h, H on the amplitude level. However, we do not consider possible interference terms between diagrams with different vector boson propagators. In other words, we approximate

$$\Gamma_{H^\pm \to 6f} \approx \Gamma(H^\pm \to [W^{\pm *} \to 2f] + [h^*/H^* \to W^*W^* \to 4f]) \tag{5.7}$$

$$+ \Gamma(H^\pm \to [W^{\pm *} \to 2f] + [h^*/H^* \to Z^*Z^* \to 4f]), \tag{5.8}$$

as is standard practice. We also define

$$\Gamma_{H^\pm \to Wh/H} \equiv \Gamma_{H^\pm \to 4f} + \Gamma_{H^\pm \to 6f}. \tag{5.9}$$

We calculate these widths using the 2HDMC implementation of our model interfaced with the tree-level matrix-element and Monte Carlo phase-space generator MadGraph [67, 68], with non-zero widths included for the internal propagators using the prescription in eq. (D.6).

As we will see in section 5.2.4, $\Gamma_{H^\pm \to Wh/H}$ is negligible in comparison to the partial widths $\Gamma_{H^\pm \to f\bar{f}'}$ and $\Gamma_{H^\pm \to W^\pm \gamma}$ for $m_{H^\pm} < m_S \lesssim 2m_W$, where S is the lightest of A and h,

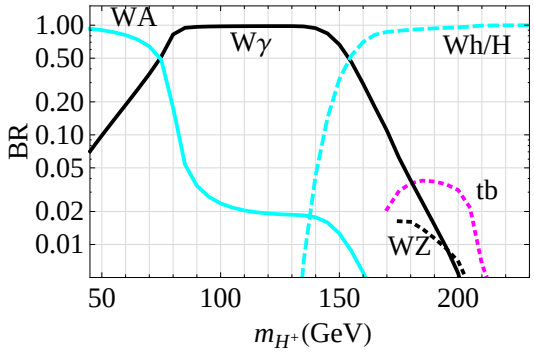

(a) $m_A = m_{H^\pm} - 10$ GeV, $m_h = 125$ GeV, $m_H = 300$ GeV, $\sin\alpha = 0.9$.

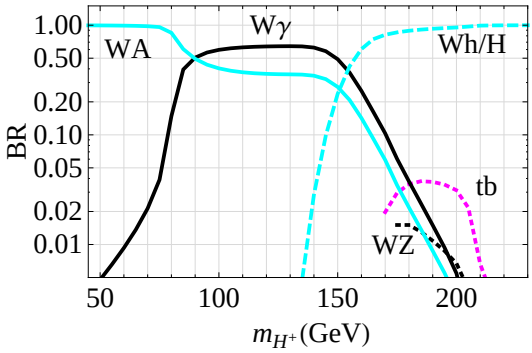

(b) $m_A = m_{H^\pm} - 20$ GeV, $m_h = 125$ GeV, $m_H = 300$ GeV, $\sin\alpha = 0.9$.

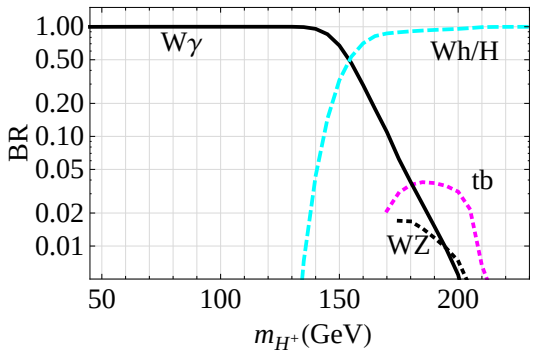

(c) $m_A = m_{H^\pm}$, $m_h = 125$ GeV, $m_H = 300$ GeV, $\sin\alpha = 0.9$.

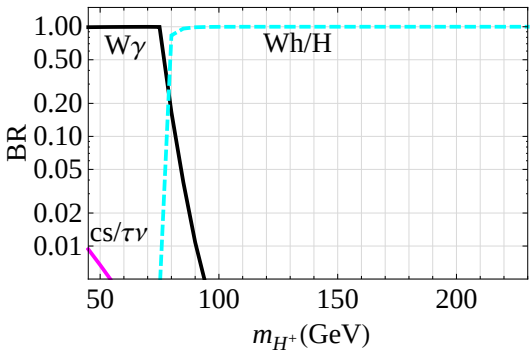

(d) $m_A = m_{H^\pm}$, $m_h = 75$ GeV, $m_H = 125$ GeV, $\sin\alpha = 0.1$.

Figure 18. The branching ratios of the charged scalar $H^\pm$ as a function of $m_{H^\pm}$. The solid black line shows the $W^\pm\gamma$ mode, dotted black $W^\pm Z$, solid cyan $W^\pm A$, dashed cyan $W^\pm h/H$ and dotted magenta tb. In this figure, we have $\lambda_3 = 2(m_{H^\pm}/v)^2$, $\lambda_2 = \lambda_1$ and $\lambda_7 = \lambda_6$. The scenarios in (a) and (b) are phenomenologically disfavored since EWPT require $m_A > m_{H^\pm}$ for these values of $m_{H^\pm}$ (see figure 4 and the related discussion).

even after the inclusion of off-shell h/H and A bosons. This is due to the smallness of the widths of the h, H and A bosons below the $h/H \to WW/ZZ$ and $A \to Zh/H$ or $W^\pm H^\mp$ thresholds. The effects of off-shell h, H and A bosons can become sizable when we consider larger $m_{h,H,A}$, i.e. when the sub-channels $h/H \to VV$ or $A \to Zh/H$ are kinematically open, so that $\Gamma_{h,H,A} = \mathcal{O}(1\text{ GeV})$. One should also remember that the $AH^\pm W^\mp$ coupling is independent of the mixing angle α.

5.2.4 Decay widths and branching ratios for $H^\pm$

We have now come to the point where we can compare the magnitudes of the different decay modes under consideration in our standard cases with $\lambda_3 = 2(m_{H^\pm}/v)^2$, $\lambda_2 = \lambda_1$ and $\lambda_7 = \lambda_6$ as is illustrated in figure 18. Here we have calculated the partial width of the decay mode $H^\pm \to W^{\pm *}A$ using the closed formulas included in 2HDMC.

First of all it should be noted that the contribution to the decay modes of $H^\pm$ from the processes $H^\pm \to \tau\nu$ and $H^\pm \to cs$ is very small: $\text{BR}(H^\pm \to \tau\nu) + \text{BR}(H^\pm \to cs) < \mathcal{O}(1\%)$. As mentioned, due to the broadness of the $W^\pm$ boson, the $H^\pm \to W^{\pm *}\gamma$ mode dominates over $H^\pm \to \tau\nu$ and $H^\pm \to cs$ even below the threshold, $m_{H^\pm} < m_W$. If one considers $m_A < m_{H^\pm}$, the decay mode $H^\pm \to W^{\pm *}A$ will start to make a significant contribution and will dominate the branching ratios for the charged scalar below the $W^\pm\gamma$ threshold, $m_{H^\pm} < m_W$. If we consider Case 1, then the mass of the A boson has to be heavier than $H^\pm$ for $m_{H^\pm} \lesssim M$ (according to the limits from EWPT illustrated in figure 4a with M given by eq. (3.2)) and the decay mode $H^\pm \to W^\pm A$ is therefore not possible for light $H^\pm$. For charged scalar masses larger than m_W, the decay mode $H^\pm \to W^\pm\gamma$ will dominate, provided that $H^\pm$ is the lightest scalar in our model. The tb and WZ modes will contribute to the branching ratios of the order a few percent.

A phenomenological consequence is that the charged scalar in our model *is not* constrained by the LEP result $m_{H^\pm} \gtrsim 80$ GeV, valid for $\text{BR}(H^\pm \to cs) + \text{BR}(H^\pm \to \tau\nu) = 1$ [47, 69, 70]. Moreover, the $W\gamma$ channel can be dominant, and WZ of order 1%. This is to be compared to the case of type-I or II 2HDMs and MSSM where the maximal branching ratios for the $W\gamma$ mode are $\sim \mathcal{O}(10^{-5})$ and $WZ \sim \mathcal{O}(10^{-3})$ [61].

Note that, as shown in figure 15, the width of $H^\pm$ can become very small in some regions of parameter space. For example, if the width would be 1 eV, then the proper decay length is $c\tau \sim 0.2\,\mu$m, and if the width is as small as 1 meV, then $c\tau \sim 0.2$ mm. It would therefore be interesting to study whether this could lead to tracks or displaced vertices in the detector. Such signatures have been studied by the CMS collaboration in [71].

5.3 Decays of the CP-odd scalar A

We end this section on scalar decays by considering the decays of the A boson. As mentioned for the $H^\pm$ bosons, we do not know *a priori* if the decay modes of the A boson into 4 or 6 fermions, via possible off-shell bosons, dominates over $A \to f\bar{f}$, which proceeds at one-loop at the lowest order in our model[4]. The decay modes of the A boson into 4 or 6 fermions through possible off-shell $h, H, H^\pm, Z$ and $W^\pm$ bosons are calculated in a very similar way as the decay of the charged scalar, in section 5.2.3.

5.3.1 $A \to f\bar{f}$

The situation here is similar to the situation for the charged scalar: the CP-odd scalar A couples to a pair of fermions with the same diagrams as the charged scalar, but with the $W^\pm$ or $G^\pm$ bosons replaced with Z or G^0 in the loop. The A bosons will mix with longitudinally polarized Z bosons (and with G^0 bosons in R_ξ gauge), which in turn go into

[4]Note that due to the quantum numbers of the A boson, the amplitudes for $A \to VV$, where $VV = W^+W^-, ZZ, \gamma\gamma, Z\gamma$ or gg, are zero at tree-level. In general 2HDMs, the A boson can couple to a pair of gauge bosons at one-loop order through a loop of fermions [72]. This is not the case in our model due to the vanishing of the tree-level couplings between A and a fermion pair, $C_{Af\bar{f}} \sim \rho^F = 0$. This means that in our model, $A \to VV$ is a two-loop process. We will not consider these decay modes in this paper.

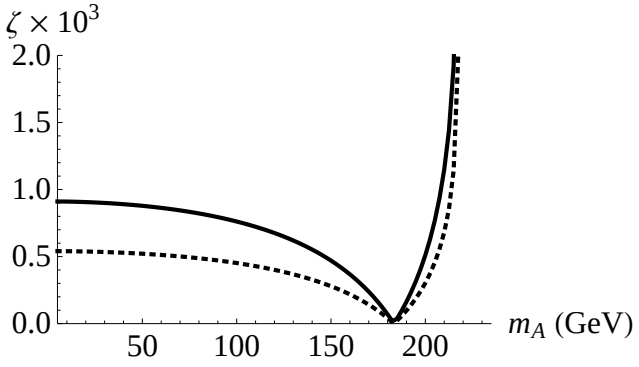

Figure 19. The ratio $\zeta = \left[\rho^L\right]_{33} / (m_\tau/v)$ as a function of m_A. The solid line is for $\sin\alpha = 0.7$ and the dotted for $\sin\alpha = 0.95$. The other parameters of the model are taken to be $m_h = 125$ GeV, $m_H = 300$ GeV, $m_{H^\pm} = m_A$.

a pair of fermions. We will renormalize the AZ and AG^0 mixing in the same way as for $H^\pm W^\pm$ and $H^\pm G^\pm$, i.e., the real part of the mixing vanishes for an on-shell A boson.

One way to give a measure of the magnitude of the loop-generated ρ^F elements in our model is by comparing e.g. $\Gamma_{A\to\tau^+\tau^-}$ calculated in our model (at one-loop level) with the tree-level result obtained in a generic model. Writing the effective interaction as $\mathrm{i}\bar{\Psi}_\tau \left[\rho^L\right]_{33} \gamma_5 \Psi_\tau \, A$, we can calculate the effective coupling $\left[\rho^L\right]_{33}$ from

$$\Gamma_{A\to\tau^+\tau^-} = \left(\left[\rho^L\right]_{33}\right)^2 \frac{m_A}{8\pi}\sqrt{1-\frac{4m_\tau^2}{m_A^2}} \ . \tag{5.10}$$

Defining the ratio

$$\zeta \equiv \frac{\left[\rho^L\right]_{33}}{m_\tau/v} \, , \tag{5.11}$$

where $\zeta = 1$ is the value obtained in a Type-I 2HDM with $\tan\beta = 1$, we find that the magnitude of ζ in our model is $\mathcal{O}(10^{-3})$ if $m_A \lesssim m_h + m_Z$, see figure 19. Note that this effective coupling is independent of the values of $m_{H^\pm}$, λ_3, λ_2, and λ_7.

Another property of the model is that at lowest order we have

$$\frac{\Gamma_{A\to c\bar{c}}}{\Gamma_{A\to s\bar{s}}} = \frac{m_c^2}{m_s^2}. \tag{5.12}$$

In this sense, our model is therefore Type I-like. Furthermore, as already mentioned, the off-diagonal entries in the ρ^F matrices are zero at one-loop level. This is due to the absence of a $W^\pm$ boson in the diagrams for the process $A \to f\bar{f}$. At two-loop order, off-diagonal ρ^F matrix elements are generated and will introduce new FCNC in our model.

5.3.2 Decay widths and branching ratios for A

The result of the calculations for the partial widths and branching ratios for the A boson is similar to those of the charged scalar. If the CP-odd scalar is not the lightest scalar in our model, the dominating decay mode is $A \to SV$, where S is the lightest scalar and

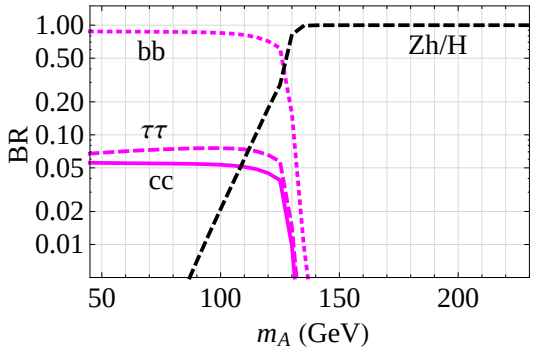

(a) $m_{H^\pm} = m_A$, $m_h = 125$ GeV, $m_H = 300$ GeV, $\sin\alpha = 0.9$.

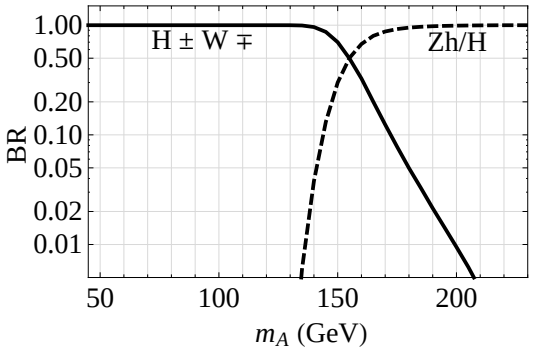

(b) $m_{H^\pm} = m_A - 45$ GeV, $m_h = 125$ GeV, $m_H = 300$ GeV, $\sin\alpha = 0.9$.

Figure 20. The various branching ratios for the scalar A: dotted magenta $A \to b\bar{b}$, solid magenta $A \to c\bar{c}$, dashed magenta $A \to \tau\tau$, dashed black $A \to Zh/H$, solid black $A \to W^\pm H^\mp$. Here $\lambda_3 = 0$, $\lambda_2 = \lambda_1$ and $\lambda_7 = \lambda_6$.

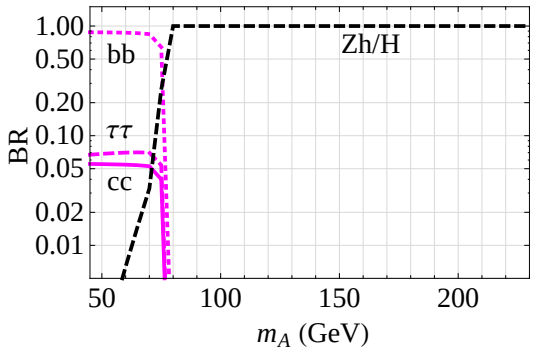

Figure 21. The branching ratios for the scalar A: dotted magenta is $b\bar{b}$, solid magenta $c\bar{c}$, dashed magenta $\tau\tau$, dashed black Zh/H. $m_{H^\pm} = m_A$, $m_h = 75$ GeV $m_H = 125$ GeV, $\sin\alpha = 0.1$. Here $\lambda_3 = 0$, $\lambda_2 = \lambda_1$ and $\lambda_7 = \lambda_6$.

V the associated vector boson. If A is the lightest scalar, the $b\bar{b}$ mode dominates, see figure 20 and figure 21. The partial decay widths $A \to f\bar{f}$ are proportional to $\sin^2 2\alpha$ and can be very small, figure 22. In Case 1 there is no region in parameter space which allows the A boson to be the lightest scalar. As was outlined in section 3, in Case 1 one should have $m_A \gtrsim m_{H^\pm} + 50$ GeV in order to fulfill the constraints from EWPT for $m_{H^\pm}$ below $m_h = 125$ GeV. In Case 2 we have larger freedom to choose m_A and $m_{H^\pm}$ according to figure 4b. But the recent LHC results restrict the possible m_A and $m_{H^\pm}$ since e.g. the decay mode $H \to AZ^*$ (with Z far off shell) should not be allowed.

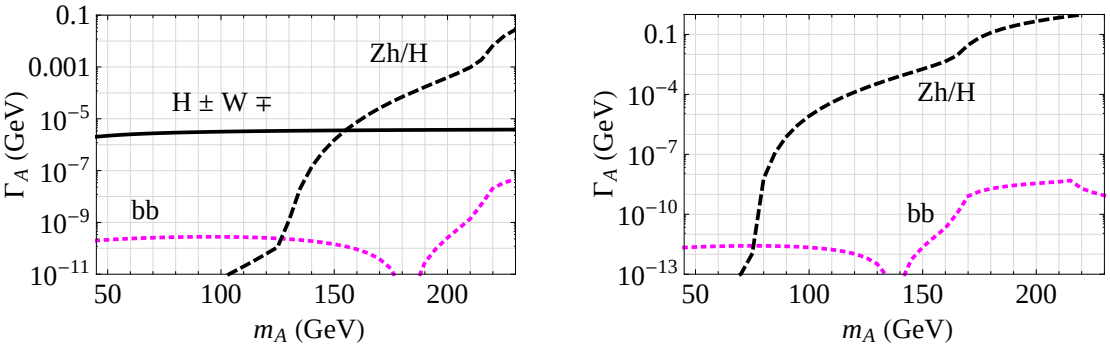

(a) $m_h = 125$ GeV, $m_H = 300$ GeV, $m_{H^\pm} = m_A - 45$ GeV, $\sin\alpha = 0.9$.

(b) $m_h = 75$ GeV, $m_H = 125$ GeV, $m_{H^\pm} = m_A$, $\sin\alpha = 0.1$.

Figure 22. The partial decay widths Γ_A as a function of m_A. Dotted magenta is $b\bar{b}$, dashed black Zh/H, solid black $W^\pm H^\mp$. Here $\lambda_3 = 0$, $\lambda_2 = \lambda_1$ and $\lambda_7 = \lambda_6$.

6 The scalars of the SDM at collider experiments

We have seen that the scalars in our model, and in particular $H^\pm$ and A, can have non-standard decay modes. If $H^\pm$ is the lightest scalar, its dominating decay mode will be $H^\pm \to W^\pm\gamma$. In this section we now consider the production of the scalars. As mentioned in section 4, the CP-even scalars h and H are produced in the same way as $H_{\rm SM}$ in gg-fusion and VBF, but with modified couplings

$$\sigma_k(pp \to H_i) = \kappa_{H_i}\,\sigma_k(pp \to H_{\rm SM}), \tag{6.1}$$

where $H_i = h, H$, $\kappa_h = \sin^2\alpha, \kappa_H = \cos^2\alpha$ and σ_k are the production cross-sections through gg-fusion or VBF.

The discovery of a charged scalar $H^\pm$ has for long been considered a sure sign of physics beyond the SM. In the standard scenarios such as MSSM, NMSSM or 2HDMs, $H^\pm$ are produced primarily in top quark decays if they are light, or if they are heavy, in association with top and bottom quarks in gg and gb collisions.

In our model, the $tbH^\pm$ coupling is zero at tree level and is instead generated by loops, and the same holds for the $Ab\bar{b}$ coupling. We have calculated the loop-generated decay width $\Gamma_{t\to H^+ b}$ in our model in the same way as we calculated $\Gamma_{H^+\to t\bar{b}}$. The result is that the branching ratio $\mathrm{BR}(t \to H^+ b)$ is less than 10^{-6} for allowed points in parameter space (the λ parameters can not be arbitrarily large). So due to the absence of tree-level fermion couplings for $H^\pm$ and A, we will neglect the standard production mechanisms of the $H^\pm$ involving the $t\bar{b}H^+$ couplings and the $gg \to A$ channel for the A. Other production mechanisms must therefore be considered. Our model thus leads to a novel phenomenology of the $H^\pm$ and A bosons, with both production and decay modes being non-standard. More detailed phenomenological studies of $H^\pm$ and A will be performed in future work, but in this section, we briefly outline some channels that will be important. Production cross sections for light charged Higgs bosons in general 2HDMs can be found in [73].

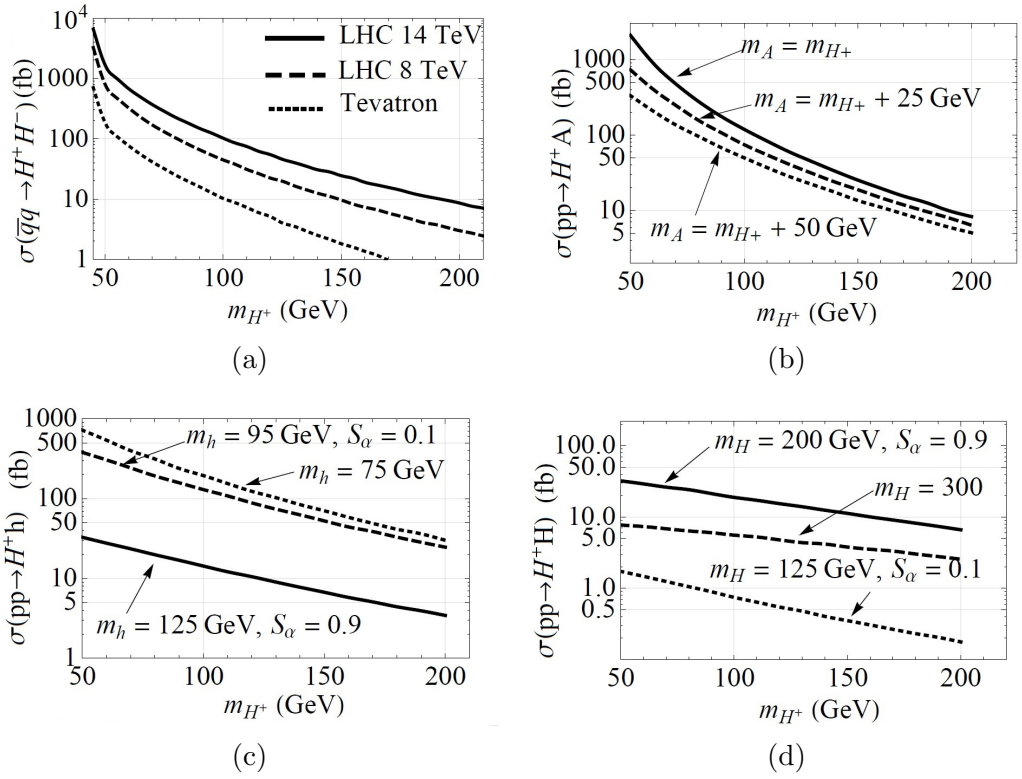

Figure 23. Hadronic cross-sections for various production mechanisms as functions of $m_{H^\pm}$: (a) $\sigma(pp \to H^+H^-)$ at LHC 8 (14) TeV solid (dashed) and $\sigma(p\bar{p} \to H^+H^-)$ at the Tevatron (dotted), (b) $\sigma(pp \to H^+A)$ at LHC 8 TeV. For the solid/dashed/dotted lines, we have $m_A = m_{H^\pm} + 0/25/50$ GeV, (c) $\sigma(pp \to H^+h)$ at LHC 8 TeV. For the solid line, we have $m_h = 125$ GeV with $\sin\alpha = 0.9$, the dashed (dotted) line $m_h = 95$ (75) GeV with $\sin\alpha = 0.1$, (d) $\sigma(pp \to H^+H)$ at LHC 8 TeV. For the solid (dashed) line, we have $m_H = 200$ (300) GeV with $\sin\alpha = 0.9$ and for the dotted line $m_H = 125$ GeV with $\sin\alpha = 0.1$.

6.1 Production of $H^\pm$

The production of a pair of charged scalars in $q\bar{q}$ collisions through s-channel γ^*/Z^* exchange depends on the electroweak couplings through the ZH^+H^- and γH^+H^- vertices. Except for the dependence on $m_{H^\pm}$, the partonic cross section for $q\bar{q} \to H^+H^-$ does not depend on the parameters of the scalar potential, if one neglects the contribution from s-channel processes with h and H bosons, whose couplings to the quarks involved are very small. To get a first estimate of the hadronic production cross sections we have calculated $\sigma(pp \to H^+H^-)$ at $\sqrt{s} = 8$ TeV and 14 TeV and $\sigma(p\bar{p} \to H^+H^-)$ at $\sqrt{s} = 2$ TeV using the LO Monte Carlo generator software MadGraph [67, 68] with CTEQ6L1 PDFs and using factorization and renormalization scales set to $\mu = M_Z$. The results are shown in figure 23a as a function of $m_{H^\pm}$.

Another production process to consider is the associated production $q\bar{q}' \to W^* \to H^\pm S$, where $S = h, H$ or A. This will give cross sections of similar magnitude as $q\bar{q} \to \gamma^*/Z^* \to H^+H^-$, provided that the sum of the final state rest masses are similar; $m_{H^\pm} +$

$m_S \approx 2m_{H^\pm}$. In figure 23b–d we show the leading order hadronic cross sections at the LHC with $\sqrt{s} = 8$ TeV, as calculated with MadGraph, for $pp \to H^+A$, $pp \to H^+h$ and $pp \to H^+H$ respectively. We note that the process $q\bar{q}' \to W^* \to H^\pm A$ is independent of the mixing angle α, whereas the $q\bar{q}' \to W^* \to H^\pm H_i$ processes have a dependence on α through the $W^\pm H^\mp H_i$ coupling, where $H_i = h, H$.

6.2 Production of A

The process $gg \to A$ occurs at two-loop level in our model. We will instead consider those regions in parameter space where it can be produced in decays of the other scalars or in association with those. If H is heavy enough, its decays $H \to AZ, AA$ could contribute a significant amount of the total production cross section of A bosons at the LHC. One could also consider the process $q\bar{q}' \to Z^* \to Ah/H$ for which the cross section is similar to the previously discussed $q\bar{q} \to H^\pm A/h/H$. One would then have to consider the subsequent decay of the A boson into hZ or $H^\pm W^\mp$. If A is the lightest scalar of the model one has to instead consider $A \to b\bar{b}$.

We also note that if A is the lightest scalar, the decay width can be very small, $\Gamma_A < 1$ meV as shown in figure 22b, for $\sin\alpha \sim 0.1$. This feature might open for signatures with displaced vertices in the detectors, provided that the A bosons are produced with sufficient p_T relative to its mass to that the γ-factor from the boost is large enough.

7 Conclusions and summary

In this paper, we have discussed a novel type of 2HDMs, first introduced by us in [14], where the $\mathbb{Z}_2$ symmetry is softly broken and only one of the doublets has a non-zero vev. This leads to that only one of the doublets has tree-level fermion couplings, and that new FCNCs occur first at the two-loop level. Since the $H^\pm$ and the A bosons reside solely in the fermiophobic doublet, indirect constraints from flavor observables do not apply. We also demonstrated that there are substantial regions of the parameter space of the model which satisfy theoretical constraints, are compatible with EWPT and earlier Higgs searches, and with the new LHC results. In particular,we have considered the $\mathcal{H} \to \gamma\gamma$ and $\mathcal{H} \to ZZ$ signal strengths, where $\mathcal{H}$ denotes the observed Higgs boson.

We have calculated the decay rates of all scalars, and in particular the decays of the $H^\pm$ and A bosons that occur through one-loop processes at lowest order. Decay modes involving off-shell final state particles have also been considered in detail. These calculations show that if the $H^\pm$ boson is the lightest scalar of the model, the non-standard decay mode $H^\pm \to W^\pm\gamma$ will normally dominate. Otherwise, decays of $H^\pm$ into on-shell scalars and off-shell vector bosons will dominate. The decay modes of the A boson show a similar behavior as for the $H^\pm$ boson. If A is not the lightest scalar, then A will decay into on-shell scalars and off-shell vector bosons. If A is the lightest scalar, $A \to b\bar{b}$ is the dominating decay channel.

Since the $H^\pm$ and A bosons of this model are fermiophobic at tree level, they have loop-suppressed standard production channels at hadron colliders. Therefore, we consider production of these scalars in pairs, and in association with vector bosons and other scalars.

These production channels could originate from $q\bar{q}'$ collisions or H decays. We estimate that, if light enough, $H^\pm$ and A should already had been produced in considerable amounts at the LHC. Therefore, more detailed investigations of such scenarios should be considered, in particular the case where $H^\pm \to W^\pm\gamma$ is the dominating decay mode.

Acknowledgments

We thank T. Hahn for being very helpful in answering questions about FeynArts and FormCalc and A. Arhrib and R. Pasechnik for helpful discussions regarding renormalization and the smeared mass unstable particle model. We also thank M. Krawczyk for helpful comments and discussions. R.E. and J.R. are supported by the Swedish Research Council under contracts 2007-4071 and 621-2011-5333.

Appendices

A Couplings

In this Appendix we give the three-particle couplings of scalars and gauge bosons. We do not list all the Goldstone boson couplings or the four-particle couplings, but these can be easily obtained using the FeynRules implementation of the model. As before, we define $s_\alpha = \sin\alpha, c_\alpha = \cos\alpha$, and $s_W = \sin\theta_W$. The triple scalar couplings of the model are then given by $g_{ijk} = -\mathrm{i}vc_{ijk}$ for $i,j,k = h, H, A, H^\pm$, where

$$c_{hhh} = 3\left(-s_\alpha^3\lambda_1 + 3c_\alpha s_\alpha^2\lambda_6 + c_\alpha^3\lambda_7 - c_\alpha^2 s_\alpha\lambda_{345}\right), \tag{A.1}$$

$$c_{HHH} = 3\left(c_\alpha^3\lambda_1 + 3c_\alpha^2 s_\alpha\lambda_6 + s_\alpha^3\lambda_7 + c_\alpha s_\alpha^2\lambda_{345}\right), \tag{A.2}$$

$$c_{hhH} = 3s_\alpha^3\lambda_6 - 3c_\alpha^2 s_\alpha\left(2\lambda_6 - \lambda_7\right) + c_\alpha s_\alpha^2\left(3\lambda_1 - 2\lambda_{345}\right) + c_\alpha^3\lambda_{345}, \tag{A.3}$$

$$c_{hHH} = 3c_\alpha^3\lambda_6 - 3c_\alpha s_\alpha^2\left(2\lambda_6 - \lambda_7\right) - c_\alpha^2 s_\alpha\left(3\lambda_1 - 2\lambda_{345}\right) - s_\alpha^3\lambda_{345}, \tag{A.4}$$

$$c_{hAA} = -s_\alpha\left(\lambda_3 + \lambda_4 - \lambda_5\right) + c_\alpha\lambda_7, \tag{A.5}$$

$$c_{HAA} = c_\alpha\left(\lambda_3 + \lambda_4 - \lambda_5\right) + s_\alpha\lambda_7, \tag{A.6}$$

$$c_{hH^+H^-} = -s_\alpha\lambda_3 + c_\alpha\lambda_7, \tag{A.7}$$

$$c_{HH^+H^-} = c_\alpha\lambda_3 + s_\alpha\lambda_7, \tag{A.8}$$

$$c_{hH^+G^-} = \frac{1}{2}\left(2s_\alpha\lambda_6 - c_\alpha(\lambda_4 + \lambda_5)\right), \tag{A.9}$$

$$c_{HH^+G^-} = -\frac{1}{2}\left(2c_\alpha\lambda_6 + s_\alpha(\lambda_4 + \lambda_5)\right). \tag{A.10}$$

Coming to the gauge–scalar couplings, we start with the SSV couplings. Writing the Feynman rules as

$$S_1S_2V \;:\; g_{S_1S_2V}(p^\mu_{S_1} - p^\mu_{S_2}), \tag{A.11}$$

where the momenta are taken to be incoming, we have

$$g_{hAZ} = \frac{ec_\alpha}{2c_W s_W}\,, \qquad g_{HAZ} = \frac{es_\alpha}{2c_W s_W}\,, \tag{A.12}$$

$$g_{hH^\pm W^\mp} = \mp\frac{\mathrm{i}ec_\alpha}{2s_W}\,, \qquad g_{HH^\pm W^\mp} = \mp\frac{\mathrm{i}es_\alpha}{2s_W}\,, \tag{A.13}$$

$$g_{AH^\pm W^\mp} = -\frac{e}{2s_W}\,, \tag{A.14}$$

$$g_{H^+H^-Z} = \frac{\mathrm{i}e\left(c_W^2 - s_W^2\right)}{2c_W s_W}\,, \qquad g_{H^+H^-\gamma} = \mathrm{i}e\,. \tag{A.15}$$

Finally we have the SVV couplings, which we write as

$$SVV \;:\; g_{SVV} g^{\mu\nu} \tag{A.16}$$

with

$$g_{hZZ} = -\frac{\mathrm{i}e^2 v s_\alpha}{2c_W^2 s_W^2}\,, \qquad g_{HZZ} = \frac{\mathrm{i}e^2 v c_\alpha}{2c_W^2 s_W^2}\,, \tag{A.17}$$

$$g_{hW^+W^-} = -\frac{\mathrm{i}e^2 v s_\alpha}{2s_W^2}\,, \qquad g_{HW^+W^-} = \frac{\mathrm{i}e^2 v c_\alpha}{2s_W^2}\,, \tag{A.18}$$

$$g_{hG^\pm W^\mp} = \pm\frac{\mathrm{i}es_\alpha}{2s_W}\,, \qquad g_{HG^\pm W^\mp} = \mp\frac{\mathrm{i}ec_\alpha}{2s_W}. \tag{A.19}$$

The gauge–scalar couplings are thus the same as in general 2HDMs with the replacement $\beta \to 0$.

B Renormalization

We here give a summary of the on-shell renormalization scheme used in [61]. The on-shell renormalization scheme at one-loop order for 2HDMs and the MSSM is also discussed in e.g. Refs. [74–78]. We renormalize the doublets and vevs according to:

$$\Phi_i \to \sqrt{Z_i}\,\hat{\Phi}_i\,, \qquad v_i \to \hat{v}_i - \delta_{v_i}\,, \tag{B.1}$$

where $v_2 = 0$ at tree level in our model, and the wavefunction renormalization constants Z_i are expanded as $Z_i = 1 + \delta_{Z_i}$ at one-loop order. These redefinitions are then inserted into the kinetic Lagrangian for the doublets. After this insertion, we obtain the following counterterms (A_μ is the photon field):

$$\delta_{H^\pm W^\mp}\,(\partial^\mu H^\pm) W_\mu^\mp\,, \tag{B.2}$$

$$\delta_{H^\pm W^\mp \gamma}\, H^\pm W_\mu^\mp A_\nu = e\delta_{H^\pm W^\mp} H^\pm W_\mu^\mp A_\nu, \tag{B.3}$$

$$\delta_{H^\pm W^\mp Z}\, H^\pm W_\mu^\mp Z_\nu = e\frac{s_W}{c_W}\delta_{H^\pm W^\mp} H^\pm W_\mu^\mp Z_\nu, \tag{B.4}$$

for the mixings and vertices respectively, where

$$\delta_{H^\pm W^\mp} = \frac{m_W}{\hat{v}_1^2 + \hat{v}_2^2}\left[\hat{v}_1\delta_{v_2} - \hat{v}_2\delta_{v_1} + \hat{v}_1\hat{v}_2(\delta_{Z_1} - \delta_{Z_2})\right]. \tag{B.5}$$

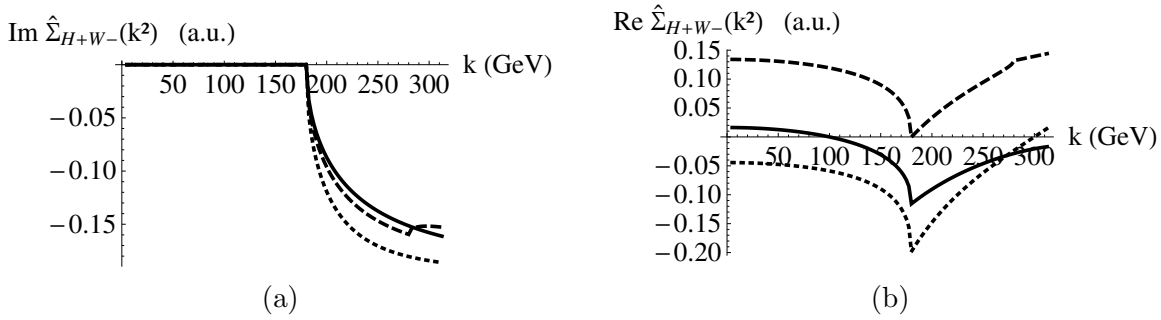

Figure 24. The imaginary part (a) and the real part (b) of the on-shell renormalized off-diagonal self energy $\hat{\Sigma}_{H^\pm W^\mp}$ as a function of the invariant mass k. In this figure we have $m_{H^\pm} = 100$ GeV (solid), $m_{H^\pm} = m_h + m_{W^\pm}$ (dashed) and $m_{H^\pm} = 300$ GeV (dotted). The other parameters in our model are taken to be $m_h = 100$ GeV, $m_H = 300$ GeV, $m_A = m_{H^\pm}$, $\sin\alpha = 0.9$, $\lambda_3 = 0$, $\lambda_2 = \lambda_1$ and $\lambda_7 = \lambda_6$.

Hence, the renormalization of the $H^\pm W^\mp Z$ and $H^\pm W^\mp \gamma$ vertices depends on the $H^\pm W^\mp$ mixing renormalization.

In order for the one-loop potential to be minimized by $\hat{v}_1$ and $\hat{v}_2$, we require that the renormalized tadpoles vanish:

$$T_{h/H} + \delta_{t_{h/H}} = 0, \tag{B.6}$$

where $T_{h/H}$ denotes the sum of all tadpole diagrams for the field h/H and $\delta_{t_{h/H}}$ the tadpole counterterms at one-loop order.

The on-shell renormalization scheme proceeds by requiring that the real part[5] of the renormalized off-diagonal self-energy $\hat{\Sigma}_{H^\pm W^\mp}$ vanishes for an on-shell $H^\pm$:

$$\mathrm{Re}\left[\hat{\Sigma}_{H^\pm W^\mp}(k^2 = m^2_{H^\pm})\right] = 0, \tag{B.7}$$

which then determines $\delta_{H^\pm W^\mp}$ according to

$$\mathrm{Re}\left[\hat{\Sigma}_{H^\pm W^\mp}(k^2 = m^2_{H^\pm})\right] = \mathrm{Re}\left[\Sigma_{H^\pm W^\mp}(k^2 = m^2_{H^\pm})\right] + \delta_{H^\pm W^\mp} = 0, \tag{B.8}$$

where the bare self-energy $\Sigma_{H^\pm W^\mp}$ is given by eq. (C.3). Furthermore, the renormalization of the $H^\pm G^\mp$ mixing is also determined by $\delta_{H^\pm W^\mp}$ due to a Slavnov–Taylor identity that forces $\hat{\Sigma}_{H^\pm W^\mp}$ and $\hat{\Sigma}_{H^\pm G^\mp}$ to be proportional to each other [61, 78, 79].

For illustration we show the real and imaginary parts of the renormalized self-energy $\hat{\Sigma}_{H^\pm W^\mp}$ in figure 24. Note that the real part vanishes for an on-shell $H^\pm$ as prescribed. Note also that the imaginary part is only non-zero when the internal particles in the loop ($W^\pm, h$ and H) can be produced on-shell, i.e. when $k > m_h + m_W$.

By following the same prescription outlined here and in [61], we find that the counterterm for AZ mixing is proportional to the one obtained for $H^\pm W^\mp$ mixing, $\delta_{AZ} = \mathrm{i}(m_Z/m_W)\,\delta_{H^\pm W^\mp}$. The AZ mixing is also defined to vanish on-shell,

$$\mathrm{Re}\left[\hat{\Sigma}_{AZ}(k^2 = m^2_A)\right] = 0\,, \tag{B.9}$$

[5] $\delta_{H^\pm W^\mp}$ is real since we consider a CP-conserving scalar sector.

and the AG^0 mixing is related to this by a similar Slavnov–Taylor identity as for the $H^\pm G^\mp$ mixing. All in all this means that the AZ and $H^\pm W^\mp$ mixing cannot vanish on-shell at the same time. At one-loop order this is not a problem since the AZ and $H^\pm W^\mp$ mixing cannot both be present in the same set of diagrams, and we are free to choose whatever scheme (i.e. values of the counterterms) we want. However, if we include two-loop diagrams, then inconsistencies may arise but this is not relevant for this study, so we leave aside the issue of on-shell renormalization of 2HDMs, and in particular of our model, at arbitrary order in perturbation theory.

In a perturbative expansion using R_ξ gauge one must also include Faddeev–Popov ghosts. The ghosts corresponding to $W^\pm$ and Z couple only to h/H in the scalar sector and only occur in loop diagrams. For diagrams that contribute to the matrix elements for $\Gamma_{H^\pm\to f\bar{f}'}$, $\Gamma_{H^\pm\to W^\pm Z/\gamma}$ and $\Gamma_{A\to f\bar{f}}$ at one loop order, the tadpole diagrams are the only ones that contain ghosts. Since we require the sum of the tadpole diagrams to vanish according to eq. (B.6) we do not need to include the ghost contributions explicitly in our calculations. It is however straightforward to include ghosts in our model. One just makes the replacement $H_{\text{SM}} \to H\cos\alpha - h\sin\alpha$ in $\mathcal{L}^{\text{SM}}_{\text{ghost}}$ [75], which gives the following couplings between ghosts (η_V) and h, H,

$$g_{h\eta_V\bar{\eta}_V} = \mathrm{i}s_\alpha\,\xi m_V^2/v\,, \quad g_{H\eta_V\bar{\eta}_V} = -\mathrm{i}c_\alpha\,\xi m_V^2/v\,, \tag{B.10}$$

where $V = W^+, W^-$ or Z.

C Expressions for the vertices and mixing self-energies

In this appendix we give the expressions for the unrenormalized vertices and self-energies. The vertex function $V_{H^+L^-\nu}$ for $H^+ \to L^+\nu$ in Feynman–'t Hooft gauge is at leading order defined as

$$\mathcal{M}_{H^+\to L^+\nu} \equiv [\bar{u}_{L^+}\,P_R\,v_\nu]V_{H^+L^-\nu}\,(m^2_{H^\pm}, m^2_L, 0\,)\,, \tag{C.1}$$

where $\mathcal{M}_{H^+\to L^+\nu}$ is the matrix element for the triangle loop contribution to $H^+ \to L^+\nu$, see figure 9b. The vertex function reads

$$\begin{aligned}
16\pi^2\,V_{H^+L^-\nu}\,(m^2_{H^\pm}, m^2_L, 0\,) \;=\;& g_{hL^+L^-}g_{hH^+W^-}\tilde{g}\,B_0(0, m^2_L, m^2_W)\\
&- g_{hL^+L^-}\left[\,g_{hH^+G^-}g_{G^+L^-\nu}m_L - g_{hH^+W^-}\tilde{g}(m^2_{H^\pm} + m^2_h - 4m^2_L)\,\right]\\
&\quad\times C_0(m^2_{H^\pm}, m^2_L, 0, m^2_W, m^2_h, m^2_L)\\
&+ g_{hL^+L^-}\left[g_{hH^+G^-}g_{G^+L^-\nu}m_L - g_{hH^+W^-}\tilde{g}\,(m^2_{H^\pm} - 2m^2_L)\,\right]\\
&\quad\times C_1(m^2_{H^\pm}, m^2_L, 0, m^2_W, m^2_h, m^2_L)\\
&+ g_{hL^+L^-}g_{hH^+W^-}\tilde{g}\,(m^2_{H^\pm} - m^2_L)\\
&\quad\times C_2(m^2_{H^\pm}, m^2_L, 0, m^2_W, m^2_h, m^2_L) + (h\to H),
\end{aligned} \tag{C.2}$$

where B_0, C_0, C_1, C_2 are Passarino–Veltman integrals [80], $\tilde{g} = \mathrm{i}e/\sqrt{2}s_W$, $g_{hL^+L^-} = \mathrm{i}m_L/v$, $g_{G^+L^-\nu} = -\mathrm{i}\sqrt{2}m_L/v$, and the remaining g_{ijk} are given in Appendix A. The $(h \to H)$ indicates the four terms that have a H boson running in the loop instead of h, which

are obtained if one makes the replacement $h \to H$. The vertex function for $H^+ u_i \bar{d}_j$ is analogous to $V_{H^+L^-\nu}$, but has more terms due to the non-vanishing quark masses.

The bare off-diagonal H^+W^- self-energy in Feynman–'t Hooft-gauge reads

$$\begin{aligned} 16\pi^2\,\Sigma_{H^+W^-}(k^2) = & \; g_{hH^+W^-}\, g_{hH^+H}\, \left[B_0(k^2, m_h^2, m_{H^\pm}^2) + 2\,B_1(k^2, m_h^2, m_{H^\pm}^2)\right] \\ & - g_{hH^+W^-}\, g_{hW^+W^-}\, \left[2\,B_0(k^2, m_h^2, m_W^2) + B_1(k^2, m_W^2, m_h^2)\right] \\ & + g_{hG^+W^-}\, g_{hH^+G^-}\, \left[B_0(k^2, m_h^2, m_W^2) + 2\,B_1(k^2, m_h^2, m_W^2)\right] \\ & + (h \to H)\,, \end{aligned} \tag{C.3}$$

where again B_0 and B_1 are Passarino–Veltman functions. The $(h \to H)$ indicates the three terms that have a H boson running in the loop instead of h are obtained if one makes the replacement $h \to H$.

One should notice that the matrix element $\mathcal{M}_{H^\pm \to W^\pm}$ for the transition $H^\pm \to W^\pm$ vanishes. This is because of the Feynman rules for the $hH^\pm W^\mp$ and $HH^\pm W^\mp$ vertices, which are present in the diagrams in figure 10:

$$SH^\pm W^\mp \; : \quad g_{SH^\pm W^\mp}\, \left[p_{H^\pm}^\mu - p_S^\mu\right], \tag{C.4}$$

where $S = h, H$ and the four-momenta are taken to be incoming. This means that the mixing diagrams are all proportional to $p_{H^\pm}^\mu = p_W^\mu$, which, combined with eq. (5.3) for a final state $W^\pm$ boson results in $\mathcal{M}_{H^\pm \to W^\pm} = 0$. A $H^\pm$ boson can therefore not fluctuate into an (on-shell) $W^\pm$ boson, which is a renormalization-scheme independent statement.

The vertex functions for $A \to 2f$ are obtained similarly. We do not give the expressions for the vertex functions for $H^\pm \to W^\pm V$ here, but they can be found in Ref. [61].

D The smeared mass unstable particle model

The smeared mass unstable particle (SMUP) model is based on the time–energy uncertainty relation and the Källén–Lehmann form of the exact propagator where finite width effects are taken into account in the spectral density, see [65, 66] and references therein. The reason we use this model is that it requires only the use and knowledge of $\Gamma^*_{H^\pm \to W^{\pm *}\gamma}(m_{H^\pm}, q)$ defined below.

To evaluate the decay width for $H^\pm \to W^{\pm *}\gamma$ for a given mass of the charged scalar, $m_{H^\pm}$, one considers the invariant mass of the virtual W, $m_{W^{\pm *}} \equiv q$, as a free parameter and defines

$$\Gamma_{H^\pm \to W^{\pm *}\gamma}(m_{H^\pm}) = \int_0^{m_{H^\pm}^2} \Gamma^*_{H^\pm \to W^{\pm *}\gamma}(m_{H^\pm}, q)\, \rho(q)\, \mathrm{d}q^2, \tag{D.1}$$

where $\Gamma^*_{H^\pm \to W^{\pm *}\gamma}(m_{H^\pm}, q)$ is the decay width for $H^\pm \to W^{\pm *}\gamma$ with the off-shell $W^\pm$ having a specific invariant mass q. This is folded with the spectral density $\rho(q)$, defined as

$$\rho(q) = \frac{1}{\pi} \frac{q\Gamma_W(q)}{[q^2 - m_W^2]^2 + [q\Gamma_W(q)]^2} \tag{D.2}$$

where we have used $m_W = 80.4$ GeV and

$$\Gamma_W(q) = \frac{9\,g^2}{48\pi} q. \tag{D.3}$$

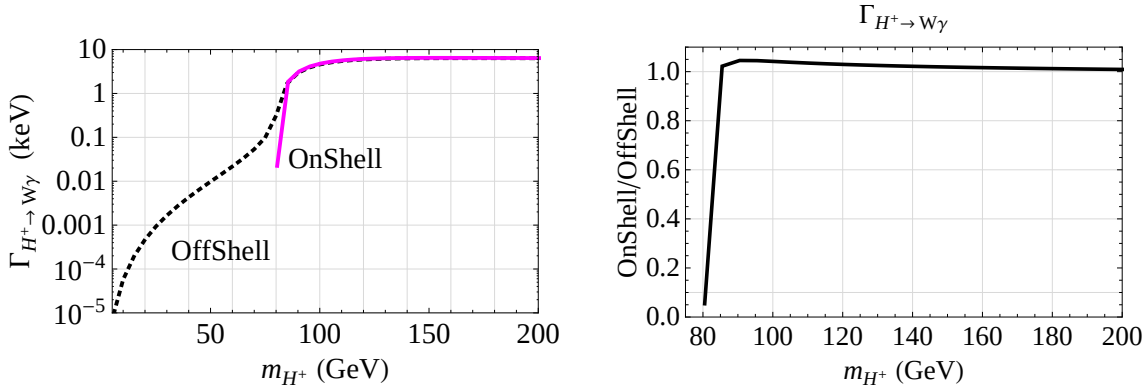

Figure 25. (a) Comparison of off-shell (dashed blue line) and on-shell (solid red line) decay widths for $H^\pm \to \gamma W^\pm$. (b) The ratio of the on-shell and the off-shell decay widths. The parameters of the model take the values $m_h = 125, m_H = 300$ GeV, $m_A = m_{H^\pm}$, $\sin\alpha = 0.9$ and $\lambda_3 = 2(m_{H^\pm}/v)^2$.

We evaluate eq. (D.1) by using our code for $H^\pm \to W^\pm\gamma$ with on-shell $W^\pm$ but allowing the $W^\pm$-mass to vary. We then integrate numerically over the spectral density.

As a check of the formalism, we also applied the SMUP model to the well-known SM process $H_{\rm SM} \to W^{-*}W^{+*}$. Comparison with known "standard" formulas [81, 82] show excellent agreement with a difference of less than 2%. The standard formula for $H_{\rm SM} \to W^{-*}W^{+*}$ with a fixed width reads [82]

$$\Gamma_{H_{\rm SM}\to W^{-*}W^{+*}}(m_{H_{\rm SM}}) = \int_0^{m^2_{H_{\rm SM}}} \frac{\mathrm{d}q_1^2\, m_W\Gamma_W/\pi}{[q_1^2 - m_W^2]^2 + m_W^2\Gamma_W^2} \int_0^{k^2} \frac{\mathrm{d}q_2^2\, m_W\Gamma_W/\pi}{[q_2^2 - m_W^2]^2 + m_W^2\Gamma_W^2}\Gamma_0 \tag{D.4}$$

where $k = m_{H_{\rm SM}} - q_1$, and

$$\Gamma_0 = \frac{m^3_{H_{\rm SM}}}{16\pi v^2}\sqrt{\left(1 - \frac{q_1^2}{m^2_{H_{\rm SM}}} - \frac{q_2^2}{m^2_{H_{\rm SM}}}\right)^2 - 4\frac{q_1^2 q_2^2}{m^4_{H_{\rm SM}}}}\left[\left(1 - \frac{q_1^2}{m^2_{H_{\rm SM}}} - \frac{q_2^2}{m^2_{H_{\rm SM}}}\right)^2 + 8\frac{q_1^2 q_2^2}{m^4_{H_{\rm SM}}}\right]. \tag{D.5}$$

This formula is obtained by denoting the denominator of the respective $W^\pm$-propagators as

$$q_i^2 - m_W^2 + \mathrm{i}m_W\Gamma_W, \tag{D.6}$$

where q_i^2 is the invariant mass squared of the i'th off-shell $W^\pm$-boson. We stress that, differently from the SMUP method, the quantity Γ_0 in (D.4) should not be literally interpreted as neither the decay width of the Higgs boson to a pair of virtual bosons with invariant masses q_1, q_2 nor as the matrix element squared.

As a further check, we evaluate $\Gamma_{H^\pm\to W^{\pm *}\gamma}$ for $m_{H^\pm}$ far above the threshold, with the result that the off-shell calculation coincides with the on-shell result, as shown in figure 25b.

References

[1] **ATLAS** Collaboration, G. Aad et al., *Observation of a new particle in the search for the Standard Model Higgs boson with the ATLAS detector at the LHC*, *Phys.Lett.* **B716** (2012) 1–29, [arXiv:1207.7214].

[2] **CMS** Collaboration, S. Chatrchyan et al., *Observation of a new boson at a mass of 125 GeV with the CMS experiment at the LHC*, *Phys.Lett.* **B716** (2012) 30–61, [arXiv:1207.7235].

[3] **CMS Collaboration** Collaboration, S. Chatrchyan et al., *Observation of a new boson with mass near 125 GeV in pp collisions at sqrt(s) = 7 and 8 TeV*, arXiv:1303.4571.

[4] **ATLAS** Collaboration, *Measurements of the properties of the higgs-like boson in the two photon decay channel with the atlas detector using 25* fb^{-1} *of proton-proton collision data*, Tech. Rep. ATLAS-CONF-2013-012, CERN, Geneva, Mar, 2013.

[5] **ATLAS** Collaboration, *Measurements of the properties of the higgs-like boson in the four lepton decay channel with the atlas detector using 25* fb^{-1} *of proton-proton collision data*, Tech. Rep. ATLAS-CONF-2013-013, CERN, Geneva, Mar, 2013.

[6] **CMS** Collaboration, *Updated measurements of the Higgs boson at 125 GeV in the two photon decay channel*, Tech. Rep. CMS-PAS-HIG-13-001, CERN, Geneva, 2013.

[7] **CMS** Collaboration, *Combination of standard model Higgs boson searches and measurements of the properties of the new boson with a mass near 125 GeV*, Tech. Rep. CMS-PAS-HIG-13-005, CERN, Geneva, 2013.

[8] G. Branco et al., *Theory and phenomenology of two-Higgs-doublet models*, *Phys.Rept.* **516** (2012) 1–102, [arXiv:1106.0034].

[9] N. G. Deshpande and E. Ma, *Pattern of Symmetry Breaking with Two Higgs Doublets*, *Phys.Rev.* **D18** (1978) 2574.

[10] E. Ma, *Verifiable radiative seesaw mechanism of neutrino mass and dark matter*, *Phys.Rev.* **D73** (2006) 077301, [hep-ph/0601225].

[11] R. Barbieri, L. J. Hall, and V. S. Rychkov, *Improved naturalness with a heavy Higgs: An Alternative road to LHC physics*, *Phys.Rev.* **D74** (2006) 015007, [hep-ph/0603188].

[12] A. Goudelis, B. Herrmann, and O. Stl, *Dark matter in the Inert Doublet Model after the discovery of a Higgs-like boson at the LHC*, *JHEP* **1309** (2013) 106, [arXiv:1303.3010].

[13] M. Krawczyk, D. Sokolowska, P. Swaczyna, and B. Swiezewska, *Constraining Inert Dark Matter by* $R_{\gamma\gamma}$ *and WMAP data*, *JHEP* **1309** (2013) 055, [arXiv:1305.6266].

[14] R. Enberg, J. Rathsman, and G. Wouda, *Higgs properties in a softly broken Inert Doublet Model*, *JHEP* **1308** (2013) 079, [arXiv:1304.1714].

[15] M. A. Diaz and T. J. Weiler, *Decays of a fermiophobic Higgs*, hep-ph/9401259.

[16] A. Akeroyd, *Fermiophobic Higgs bosons at the Tevatron*, *Phys.Lett.* **B368** (1996) 89–95, [hep-ph/9511347].

[17] A. Akeroyd, *Fermiophobic and other nonminimal neutral Higgs bosons at the LHC*, *J.Phys.G* **G24** (1998) 1983–1994, [hep-ph/9803324].

[18] A. Barroso, L. Brucher, and R. Santos, *Is there a light fermiophobic Higgs?*, *Phys.Rev.* **D60** (1999) 035005, [hep-ph/9901293].

[19] L. Brucher and R. Santos, *Experimental signatures of fermiophobic Higgs bosons*, *Eur.Phys.J.* **C12** (2000) 87–98, [hep-ph/9907434].

[20] E. Gabrielli and B. Mele, *A Radiatively improved fermiophobic Higgs boson scenario*, arXiv:1112.5993. 7 pages, 3 figures, Proceedings of the 2011 International Workshop on Future Linear Colliders (LCWS11), Granada (Spain), 26-30 September 2011.

[21] E. Gabrielli, B. Mele, and M. Raidal, *Has a Fermiophobic Higgs Boson been Detected at the LHC ?*, *Phys.Lett.* **B716** (2012) 322–325, [arXiv:1202.1796].

[22] A. Celis, V. Ilisie, and A. Pich, *Towards a general analysis of LHC data within two-Higgs-doublet models*, arXiv:1310.7941.

[23] L. Lavoura, *Signatures of discrete symmetries in the scalar sector*, *Phys.Rev.* **D50** (1994) 7089–7092, [hep-ph/9405307].

[24] S. Davidson and H. E. Haber, *Basis-independent methods for the two-Higgs-doublet model*, *Phys. Rev.* **D72** (2005) 035004, [hep-ph/0504050]. *Erratum:* Phys. Rev. **D72** 099902 (2005).

[25] I. Ivanov, *Two-Higgs-doublet model from the group-theoretic perspective*, *Phys.Lett.* **B632** (2006) 360–365, [hep-ph/0507132].

[26] H. E. Haber and D. O'Neil, *Basis-independent methods for the two-Higgs-doublet model. II: The significance of tan(beta)*, *Phys. Rev.* **D74** (2006) 015018, [hep-ph/0602242]. *Erratum:* Phys. Rev. **D74** 059905(E) (2006).

[27] J. Mrazek, A. Pomarol, R. Rattazzi, M. Redi, J. Serra, et al., *The Other Natural Two Higgs Doublet Model*, *Nucl.Phys.* **B853** (2011) 1–48, [arXiv:1105.5403].

[28] M. Ambroso, V. Braun, and B. A. Ovrut, *Two Higgs Pair Heterotic Vacua and Flavor-Changing Neutral Currents*, *JHEP* **0810** (2008) 046, [arXiv:0807.3319].

[29] G. Wouda, *Charged scalars in a lopsided doublet model*, *PoS* **CHARGED2010** (2010) 032.

[30] S. L. Glashow and S. Weinberg, *Natural Conservation Laws for Neutral Currents*, *Phys. Rev.* **D15** (1977) 1958.

[31] E. Paschos, *Diagonal Neutral Currents*, *Phys.Rev.* **D15** (1977) 1966.

[32] J. F. Gunion and H. E. Haber, *The CP-conserving two-Higgs-doublet model: The approach to the decoupling limit*, *Phys. Rev.* **D67** (2003) 075019, [hep-ph/0207010].

[33] M. Sher, *Electroweak Higgs Potentials and Vacuum Stability*, *Phys. Rept.* **179** (1989) 273–418.

[34] D. Eriksson, J. Rathsman, and O. Stål, *2HDMC: Two-Higgs-Doublet Model Calculator Physics and Manual*, *Comput.Phys.Commun.* **181** (2010) 189–205, [arXiv:0902.0851].

[35] D. Eriksson, J. Rathsman, and O. Stål, *2HDMC: Two-Higgs-doublet model calculator*, *Comput.Phys.Commun.* **181** (2010) 833–834.

[36] H. Huffel and G. Pocsik, *Unitarity bounds on Higgs boson masses in the Weinberg-Salam model with two Higgs doublets*, *Zeit. Phys.* **C8** (1981) 13.

[37] J. Maalampi, J. Sirkka, and I. Vilja, *Tree level unitarity and triviality bounds for two Higgs models*, *Phys. Lett.* **B265** (1991) 371–376.

[38] S. Kanemura, T. Kubota, and E. Takasugi, *Lee-Quigg-Thacker bounds for Higgs boson masses in a two doublet model*, *Phys. Lett.* **B313** (1993) 155–160, [hep-ph/9303263].

[39] A. G. Akeroyd, A. Arhrib, and E.-M. Naimi, *Note on tree-level unitarity in the general two Higgs doublet model*, *Phys. Lett.* **B490** (2000) 119–124, [hep-ph/0006035].

[40] I. F. Ginzburg and I. P. Ivanov, *Tree-level unitarity constraints in the most general 2HDM*, *Phys. Rev.* **D72** (2005) 115010, [hep-ph/0508020].

[41] J. Bijnens, J. Lu, and J. Rathsman, *Constraining General Two Higgs Doublet Models by the Evolution of Yukawa Couplings*, *JHEP* **1205** (2012) 118, [arXiv:1111.5760].

[42] A. Barroso, P. Ferreira, I. Ivanov, R. Santos, and J. P. Silva, *Evading death by vacuum*, arXiv:1211.6119.

[43] A. Barroso, P. Ferreira, I. Ivanov, and R. Santos, *Metastability bounds on the two Higgs doublet model*, *JHEP* **1306** (2013) 045, [arXiv:1303.5098].

[44] M. E. Peskin and T. Takeuchi, *Estimation of oblique electroweak corrections*, *Phys. Rev.* **D46** (1992) 381–409.

[45] **Particle Data Group** Collaboration, J. e. a. Beringer, *Review of particle physics*, *Phys. Rev. D* **86** (Jul, 2012) 010001.

[46] F. Mahmoudi and O. Stål, *Flavor constraints on the two-Higgs-doublet model with general Yukawa couplings*, *Phys.Rev.* **D81** (2010) 035016, [arXiv:0907.1791].

[47] **DELPHI Collaboration** Collaboration, J. Abdallah et al., *Search for charged Higgs bosons at LEP in general two Higgs doublet models*, *Eur.Phys.J.* **C34** (2004) 399–418, [hep-ex/0404012].

[48] P. Bechtle, O. Brein, S. Heinemeyer, G. Weiglein, and K. E. Williams, *HiggsBounds: Confronting Arbitrary Higgs Sectors with Exclusion Bounds from LEP and the Tevatron*, *Comput. Phys. Commun.* **181** (2010) 138–167, [arXiv:0811.4169].

[49] P. Bechtle, O. Brein, S. Heinemeyer, G. Weiglein, and K. E. Williams, *HiggsBounds 2.0.0: Confronting Neutral and Charged Higgs Sector Predictions with Exclusion Bounds from LEP and the Tevatron*, *Comput. Phys. Commun.* **182** (2011) 2605–2631, [arXiv:1102.1898].

[50] A. Arhrib, R. Benbrik, and N. Gaur, $H \to \gamma\gamma$ *in Inert Higgs Doublet Model*, *Phys.Rev.* **D85** (2012) 095021, [arXiv:1201.2644].

[51] B. Swiezewska and M. Krawczyk, *Diphoton rate in the Inert Doublet Model with a 125 GeV Higgs boson*, *Phys.Rev.* **D88** (2013) 035019, [arXiv:1212.4100].

[52] C.-W. Chiang and K. Yagyu, *Implications of Higgs boson search data on the two-Higgs doublet models with a softly broken Z_2 symmetry*, *JHEP* **1307** (2013) 160, [arXiv:1303.0168].

[53] **ATLAS** Collaboration, *Combined measurements of the mass and signal strength of the higgs-like boson with the atlas detector using up to 25 fb^{-1} of proton-proton collision data*, Tech. Rep. ATLAS-CONF-2013-014, CERN, Geneva, Mar, 2013.

[54] P. Bechtle, O. Brein, S. Heinemeyer, O. Stål, T. Stefaniak, et al., *HiggsBounds-4: Improved Tests of Extended Higgs Sectors against Exclusion Bounds from LEP, the Tevatron and the LHC*, arXiv:1311.0055.

[55] P. Bechtle, O. Brein, S. Heinemeyer, O. Stål, T. Stefaniak, et al., *Recent Developments in HiggsBounds and a Preview of HiggsSignals*, *PoS* **CHARGED2012** (2012) 024, [arXiv:1301.2345].

[56] P. Bechtle, S. Heinemeyer, O. Stål, T. Stefaniak, and G. Weiglein, *HiggsSignals: Confronting arbitrary Higgs sectors with measurements at the Tevatron and the LHC*, arXiv:1305.1933.

[57] T. Hahn, *Generating Feynman diagrams and amplitudes with FeynArts 3*, *Comput. Phys. Commun.* **140** (2001) 418–431, [hep-ph/0012260].

[58] T. Hahn and M. Perez-Victoria, *Automatized one-loop calculations in four and D dimensions*, *Comput. Phys. Commun.* **118** (1999) 153–165, [hep-ph/9807565].

[59] T. Hahn and M. Perez-Victoria, *Automatized one loop calculations in four-dimensions and D-dimensions*, *Comput.Phys.Commun.* **118** (1999) 153–165, [hep-ph/9807565].

[60] N. D. Christensen and C. Duhr, *FeynRules - Feynman rules made easy*, *Comput.Phys.Commun.* **180** (2009) 1614–1641, [arXiv:0806.4194].

[61] A. Arhrib, R. Benbrik, and M. Chabab, *Charged Higgs bosons decays $H^{\pm} \to W^{\pm}(\gamma, Z)$ revisited*, *J.Phys.* **G34** (2007) 907–928, [hep-ph/0607182].

[62] E. Braaten and J. Leveille, *Higgs Boson Decay and the Running Mass*, *Phys.Rev.* **D22** (1980) 715.

[63] M. Drees and K.-i. Hikasa, *Note on QCD corrections to hadronic Higgs decay*, *Phys.Lett.* **B240** (1990) 455.

[64] S. Gorishnii, A. Kataev, S. Larin, and L. Surguladze, *Three-loop QCD correction to the correlator of the quark scalar currents and $\Gamma_{tot}(H^0 \to hadrons)$*, *Mod.Phys.Lett.* **A5** (1990) 2703–2712.

[65] V. Kuksa and R. Pasechnik, *Near-threshold W-pair production in the model of unstable particles with smeared mass*, *Int.J.Mod.Phys.* **A24** (2009) 5765–5777, [arXiv:0902.2857].

[66] R. S. Pasechnik and V. I. Kuksa, *Finite-width effects in the near-threshold ZZZ and ZWW production at ILC*, *Mod.Phys.Lett.* **A26** (2011) 1075–1093, [arXiv:1011.4202].

[67] J. Alwall, P. Demin, S. de Visscher, R. Frederix, M. Herquet, et al., *MadGraph/MadEvent v4: The New Web Generation*, *JHEP* **0709** (2007) 028, [arXiv:0706.2334].

[68] J. Alwall, M. Herquet, F. Maltoni, O. Mattelaer, and T. Stelzer, *MadGraph 5 : Going Beyond*, *JHEP* **1106** (2011) 128, [arXiv:1106.0522].

[69] **ALEPH Collaboration** Collaboration, A. Heister et al., *Search for charged Higgs bosons in e^+e^- collisions at energies up to $\sqrt{s}$ = 209 GeV*, *Phys.Lett.* **B543** (2002) 1–13, [hep-ex/0207054].

[70] **ALEPH Collaboration, DELPHI Collaboration, L3 Collaboration, OPAL Collaboration, The LEP working group for Higgs boson searches** Collaboration, G. Abbiendi et al., *Search for Charged Higgs bosons: Combined Results Using LEP Data*, *Eur.Phys.J.C* (2013) [arXiv:1301.6065].

[71] **CMS Collaboration** Collaboration, S. Chatrchyan et al., *Searches for long-lived charged particles in pp collisions at $\sqrt{s}$=7 and 8 TeV*, arXiv:1305.0491.

[72] A. Arhrib and R. Benbrik, *Searching for a CP-odd Higgs via a pair of gauge bosons at the LHC*, hep-ph/0610184.

[73] M. Aoki, R. Guedes, S. Kanemura, S. Moretti, R. Santos, et al., *Light Charged Higgs bosons at the LHC in 2HDMs*, *Phys.Rev.* **D84** (2011) 055028, [arXiv:1104.3178].

[74] A. Dabelstein, *The One loop renormalization of the MSSM Higgs sector and its application to the neutral scalar Higgs masses*, *Z.Phys.* **C67** (1995) 495–512, [hep-ph/9409375].

[75] R. Santos and A. Barroso, *On the renormalization of two Higgs doublet models*, *Phys.Rev.* **D56** (1997) 5366–5385, [hep-ph/9701257].

[76] A. Arhrib, M. Capdequi Peyranere, W. Hollik, and G. Moultaka, *Associated H^-W^+ production in high-energy e^+e^- collisions*, *Nucl.Phys.* **B581** (2000) 34–60, [hep-ph/9912527].

[77] H. E. Logan and S.-f. Su, *Associated production of $H^\pm$ and $W^\mp$ in high-energy e^+e^- collisions in the minimal supersymmetric standard model*, *Phys.Rev.* **D66** (2002) 035001, [hep-ph/0203270].

[78] D. Lopez-Val and J. Sola, *Neutral Higgs-pair production at Linear Colliders within the general 2HDM: Quantum effects and triple Higgs boson self-interactions*, *Phys.Rev.* **D81** (2010) 033003, [arXiv:0908.2898].

[79] J. A. Coarasa Perez, D. Garcia, J. Guasch, R. A. Jimenez, and J. Sola, *Quantum effects on $t \to H^+b$ in the MSSM: A Window to 'virtual' supersymmetry?*, *Eur.Phys.J.* **C2** (1998) 373–392, [hep-ph/9607485].

[80] G. Passarino and M. Veltman, *One Loop Corrections for e^+e^- Annihilation Into $\mu^+\mu^-$ in the Weinberg Model*, *Nucl.Phys.* **B160** (1979) 151.

[81] J. C. Romao and S. Andringa, *Vector boson decays of the Higgs boson*, *Eur.Phys.J.* **C7** (1999) 631–642, [hep-ph/9807536].

[82] A. Djouadi, *The Anatomy of electro-weak symmetry breaking. I: The Higgs boson in the standard model*, *Phys.Rept.* **457** (2008) 1–216, [hep-ph/0503172].